Journal of Materials Research and Technology 28 (2024) 1433–1451

Contents lists available at ScienceDirect

Journal of Materials Research and Technology

journal homepage: www.elsevier.com/locate/jmrt

Assessing underdeposit corrosion inhibitor performance for carbon steel in CO_2/Sulfide environment

Eman M. Fayyad [a,**,1], Mostafa H. Sliem [a], Noora Al-Qahtani [a], Mary P. Ryan [b], Aboubakr M. Abdullah [a,*]

[a] Center for Advanced Materials, Qatar University, Doha, 2713, Qatar
[b] Department of Materials, Imperial College Exhibition Road, London, SW72AZ, UK

ARTICLE INFO

Handling editor: P.Y. Chen

Keywords:
UDC inhibitor
Deposits
Sweet/sour conditions
Under-deposit corrosion
Carbon steel

ABSTRACT

Under deposit corrosion (UDC) that occurs due to the deposition of solid particles, like iron sulfide or organic solids, and CO_2 corrosion, cause disasters for pipelines and fluid-handling apparatus. This research investigated the impact of mineral deposits, like iron disulfide, iron sulfide, and sand, on the inhibition performance of the commercial UDC inhibitor in sulfated CO_2-saturated brine solution at 60 °C and 1000 rpm flow rates for different immersion times. The deposit characteristics, type, and coverage technique on the steel (full/partial) were explored. The surface morphology, elemental analysis, and particle size of deposits in the absence and presence of the inhibitor were analyzed. The inhibitive effect at different inhibitor concentrations and the corrosion rates of steel in the absence and presence of the deposits were calculated from the fitting process of the electrochemical impedance spectroscopy (EIS) results. The utilized UDC inhibitor has the highest efficiency (about 95 %) at a concentration of 400 ppm. The FeS, FeS_2 and SiO_2 deposits in the presence of the inhibitor offered a 77.5 %, 94.5 % and 94.6 % inhibition efficiency after 6h of immersion time, resulting in about 77.5 %, 25.6 % and 60.1 % increase in their efficiencies before the addition of the inhibitor. Therefore, the inhibitor can effectively inhibit the UDC triggered by FeS and SiO_2 deposits in an aqueous environment containing sulfated CO_2. However, it is unavailable in the steel underneath the FeS_2 deposit to inhibit corrosion. EDX and XPS analyses confirm the success of the inhibitor movement through deposits and its adsorption on steels.

1. Introduction

Oilfields utilize J55 carbon steel for the casing of the pipes and as part of the wellbores. As a result of J55 carbon steel being cost-effective compared to other steels, it is commonly used in many applications [1]. The presence of carbon dioxide causes sweet corrosion, which is a primary concern for the gas and oil industries. It is known that impurities such as hydrogen sulfide and carbon dioxide in the crude oil in the reservoirs are present [2]. An additional source of water and carbon dioxide in the reservoir is the formation of water inserted into the reservoir to cause stability and pressure to rise [3–5]. Severe steel corrosion occurs from the production of carbonic acid due to the buildup of water and carbon dioxide [6,7]. In addition, hydrogen revolution, which is a cathodic reaction, and iron dissolution, which is an anodic reaction, are accelerated in the occurrence of hydrogen sulfide. Thus, the rate of iron corrosion in acidic environments increases. As a result, it is pivotal to have a solution for the corrosion protection of hydrogen sulfide in steel pipelines and equipment [8–10]. However, there is a limit in lab results due to the toxic nature of hydrogen sulfide, and its corrosion effect on some carbon steel has been reported on a laboratory scale with high facilities [11]. Furthermore, many gas and oil fields have deposits, which amass on the inner surface of the pipelines when there is a decreased flow rate or shutdown times. This causes a phenomenon known as under-deposit corrosion (UDC) [12–14]. UDC is known to be an extremely aggressive form of internal corrosion, which further increases the rate of the deterioration of the pipelines. A range of different cases and failures have been reported, which originate from the UDC of metallic structures. UDC caused the failure of the sodium carbonate transportation pipeline, as shown by Almahamedh et al. [15], and ammonium chloride UDC caused the breakdown of s special tube, as

* Corresponding author.
** Corresponding author.
E-mail addresses: emfayad@qu.edu.qa (E.M. Fayyad), bakr@qu.edu.qa (A.M. Abdullah).
[1] Permanent address: Physical Chemistry Department, National Research Centre, P.O. Box 12622, Dokki, Cairo, Egypt.

https://doi.org/10.1016/j.jmrt.2023.11.244
Received 4 January 2023; Received in revised form 4 May 2023; Accepted 26 November 2023
Available online 10 December 2023

directed by Zhu et al. [16]. The type of deposit and the environment highly influence the mechanism of the UDC [17,18]. Organic deposits, such as asphaltene, wax, biofilms, inorganic deposits, such as sand and corrosion products, and a combination of both are all produced in gas and oil facilities [19]. The compositions and properties of these deposits rely on both the initial oil source and the technical attributes of the pipelines and transportation procedures [20].

Iron sulfide is well known to be electrochemically active and semiconductive, while sand is electrochemically inactive and inert [21]. The different iron sulfides, which have six modifications, have various properties [22]. The environmental conditions can influence the modifications from changing from one to another. Due to gravity, most deposits accumulate at the cylindrical surface's bottom. This leads to the highest surface area of the metal that is not under the deposit. Therefore, different anodic and cathodic regions are produced in the pipelines, which also affects the corrosion mechanism [23]. The utilization of corrosion inhibitors to modify the sweet corrosive environment can be an appropriate solution to the problem [24–30]. Organic compounds are the preferred type of UDC inhibitors over inorganic ones, possibly due to the drawbacks of low efficiency and high concentration of inorganic corrosion inhibitors [31]. Unfortunately, the market does not have any inhibitors designed specifically for UDC in a sour environment despite the massive increase of UDC corrosion inhibitors. Globally, over 40 % of gas reservoirs are sour, hence, containing significant levels of hydrogen sulfide [32]. Thus, the development and production of corrosion inhibitors for such an application are difficult due to the inhibitor adsorption and diffusion by deposits. The range of corrosion inhibitors available is large because of the vast market. Thus, to select the best corrosion inhibitor, qualification testing is done in labs [33,34].

The purpose of this work is to study the performance of UDC commercial inhibitor in absence and presence of the deposits in sweet and sour media. Therefore, firstly, the influence of different types of laboratory deposits, namely, iron sulfide (FeS), iron disulfide (FeS_2), and sand, on the corrosion of J55 carbon steel was studied in the absence of the inhibitor, for different immersion times (0, 6, 12 and 24 h), in 3.5 wt % NaCl that is purged with CO_2 for saturation, and contained 1000 ppm Na_2S to simulate the presence of H_2S, at an elevated temperature (60 °C) with 1000 rpm rotation of the working electrode to simulate, to some extent, the oilfield pipeline's environment [35,36]. In addition, the impact of the coverage method, either full or partial, of each deposit on the steel was illustrated. Secondly, the corrosion inhibition ability of the different concentrations (5, 10, 25, 50, 100, 200, 300, 400, and 500 ppm) of the inhibitor, which is amine salt of organic phosphates and is abbreviated as CR11, under the aforementioned conditions was evaluated in the absence of the deposits. After that, the performance of the inhibitor was examined in the presence of each deposit that is either fully or partially covered the steel, for different immersion times. The obtained best inhibitor concentration (optimum concentration) is utilized in this stage. All the electrochemical studies were done using electrochemical impedance spectroscopy (EIS). The SEM, EDX, and XPS characterize the deposits, and the deposited as well as the inhibited steel after 24 h immersion time.

2. Experimental techniques

2.1. Chemicals and materials

J55 pipeline steel (provided by Qatar Shell) is machined in a rod shape with 5 mm diameter and 50 mm length. Then, it is mounted in cold mounting epoxy resin to prevent the ingress of test solutions into the sides of the electrodes. Different grits (up to 4000 grits) of emery paper were used to refine the steel specimens' surfaces. Then, the specimens are degreased by rinsing with acetone and deionized water before the reaction. The chemical composition of the J55 steel is as follows in weight percent (wt. %); C: 0.29; Si: 0.33; Mn: 1.30; Cr: 0.06; Mo: 0.04; S: 0.001; P: 0.009; Ni: 0.02; Cu: 0.02 and the balance; Fe.

All solutions have been prepared from pure reagents procured from Sigma-Aldrich (St. Louis, MO, USA). The test solution was prepared using ultra-pure water (Mili-Q system, resistivity 18.2 MX cm) and consisted of 3.5 wt % NaCl and 1000 ppm Na_2S. The addition of 1000 ppm Na_2S simulates the concentration of the sulfide residue, which ranges from 200 to 500 ppm that is found in the oil and gas pipelines. The test sulfated brine solution was saturated with CO_2 and its temperature was adjusted to 60 °C. In addition, the working electrode was rotated at 1000 rpm in all experiments. A commercial inhibitor, which is amine salts of organic phosphates, including mercapto 2-methylimidazole, is used. For simplification, the inhibitor is referred to as CR11. The corrosion inhibitor was used as received without treatment. The corrosion inhibitor was added in various concentrations ranging from 5 to 500 ppm to the test sulfated brine solution to prepare the inhibited one. Three different deposits, iron sulfide (FeS), iron disulfide (FeS_2), and sand (SiO_2), with a mesh of 100 (149 μ), 325 (44 μ), 230 (62 μ), respectively, were purchased from Sigma Aldrich, UK, were utilized to imitate the formed deposits in the pipeline.

2.2. Deposit preparation

For the deposits application, 0.3 mg of the required material in a mixture of 0.6 mL isopropyl alcohol and 0.4 mL Nafion (5 wt %) was dispersed. After that, the solution was sonicated for 2 h. Then, 10 μL of the dispersion deposit was cast on the J55 steel surface and allowed to dry for 2 h. Thereafter, the prepared electrode is laid at 80 °C for 4h to make a compact deposit layer. Two protocols (coverage methods) were used for depositing the deposit on the electrode surface: either full or partial coverage.

2.3. Electrochemical measurements

A double-jacketed cell containing three electrodes is utilized in the electrochemical measurements. The J55 steel with an exposed area of 0.5 mm is the working electrode, the graphite rod is the counter electrode, and a silver/silver chloride electrode (Ag/AgCl) represents the reference electrode. To ensure an appropriate geometry of cell electrodes to minimize the potential drop, a lugging capillary was associated with the reference electrode. A Julabo F12 thermostat was used to regulate the temperature of the test solution. Fig. 1 is a photo of the experimental setup. Electrochemical impedance spectroscopy (EIS) is employed to evaluate the different electrochemical parameters. Before each EIS measurement, the carbon steel was dipped in the test solution for 30 s to achieve the chemical interaction of the steel with the electrolyte solution. The EIS analysis was accomplished using GAMRY 3000 potentiostat/galvanostat/ZRA after attaining an open circuit potential (OCP) in the frequency range of 0.1 Hz–100 kHz and with 10 mV AC amplitude. To ensure the reproducibility of the measurements, each test was repeated three times, and the values were averaged.

2.4. Surface morphology and characterization

The morphology, distribution, and elemental analysis of the three different deposits on the carbon steel in the presence and absence of the inhibitor were analyzed using a scanning electron microscope (SEM), which is called Nova NanoSEM 450 from ThermoFisher Scientific company in Eindhoven-Netherlands. The SEM joined with the energy-dispersive X-ray spectroscopy (EDX) equipment with Bruker detector 127 eV, which is from Bruker, Leiderdorp, Netherlands.

To compare the chemistry surfaces of the as-prepared deposits and the inhibited deposits-covered specimens, the XPS analysis was achieved using ESCALAB 250X equipment, which is from ThermoFisher Scientific, Waltham, MA, USA. The XPS was done with 1 eV energy resolution and AlKα excitation radiation (25W, hυ = 1486.5 eV).

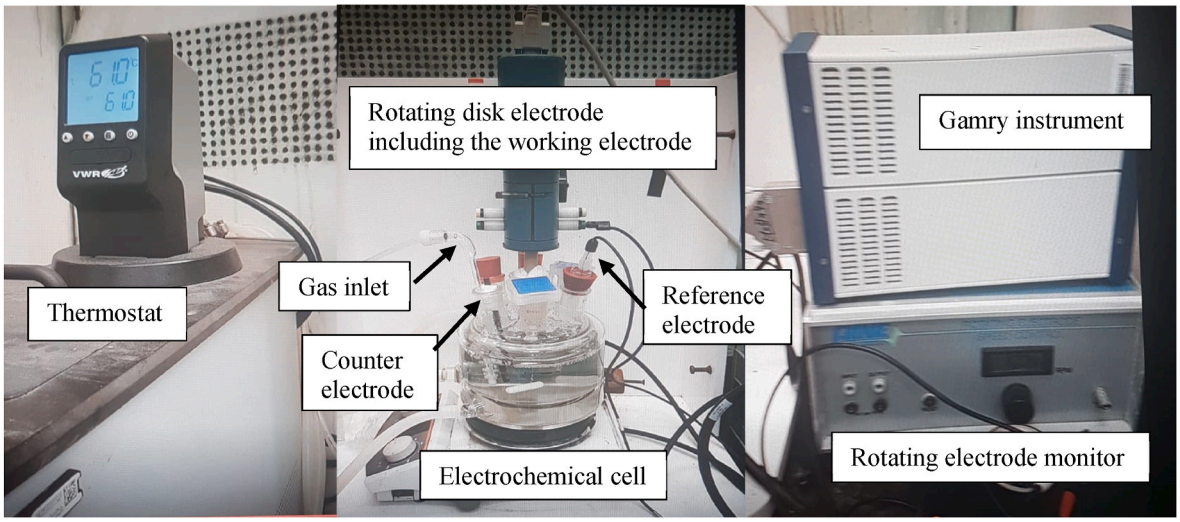

Fig. 1. A photo of the experimental setup.

3. Results and discussion

3.1. Electrochemical measurements

EIS technique is the most informative method for explaining the electrode/electrolyte interface interactions, expressing the corrosion behavior, and calculating its rate [37,38] over wide ranges of frequencies and throughout in-situ and non-destructive probing relaxation phenomena. Therefore, using EIS, we assess the impacts of different deposits (FeS, FeS_2, and SiO_2) on the corrosion of the J55 steel, which has an exposed surface area of 0.2 cm^2, in sulfated CO_2-saturated brine solution at high temperature (60 °C) and rotation of 1000 rpm in the absence and presence of the inhibitor to evaluate its performance in the presence of the deposits. In addition, the performance of the different concentrations of commercial inhibitor (CR11) under the previous conditions for different immersion times was evaluated. The resulting experimental data will be analyzed and fitted using the suitable equivalent circuits for each system that will be later described. It is worth mentioning that the following equations are used to calculate the surface coverage θ and the inhibition efficiency (IE %) of the inhibitor [39,40];

$$\theta = \frac{R_{2\ (inh\ CS)} - R_{2(CS)}}{R_{2\ (inh\ CS)}} \times 100 \quad (1)$$

$$\text{IE } \% = \theta \times 100 \quad (2)$$

where $R_{2\ (inh\ CS)}$ and $R_{2\ (CS)}$ are the charge transfer resistances of the inhibited/sand deposited carbon steel and the bare carbon steel, respectively, in the test sulfated CO_2-saturated brine solution.

Moreover, the corrosion rate in mm/year can be calculated using the equation below [41–43]:

$$CR = \frac{3.28\ I_{corr}\ M}{\rho . n} \quad (3)$$

where CR is the corrosion rate (mm/year), I_{corr} is the corrosion current in mA/cm^2, M is the molar mass of iron, which is equal to 56 g/mol, ρ its volume density, which is equal to 7.87 g/cm^3, and n = 2, which is the number of electrons freed by the corrosion reaction. The corrosion current (I_{corr}) can be calculated using the Stern-Geary equation [44]:

$$I_{corr} = \frac{B}{R_{ct}} \text{ x } 1000 \quad (4)$$

where B is the stern constant, which is equal to 0.026 V, and R_{ct} is the charge transfer resistance in Ω.cm^2.

3.1.1. The performance of deposits (types and coverage method)

The Nyquist and Bode plots of the EIS results for the bare steel (control sample) immersed in sulfated CO_2-saturated brine solution, for different immersion times (0, 6, 12, and 24h), at 60 °C with 1000 rpm rotation are illustrated in Fig. 2. Whereas, Fig. 3 represents the Nyquist plots (a, b, and c), and their corresponding Bode plots (a', b', and c') of the EIS results for the partial-deposited steels with different deposits (FeS, FeS_2, and SiO_2) that are immersed in the previous electrolyte under the same conditions for different immersion times. Moreover, EIS results for the corresponding full-deposited steel specimens with different deposits under the same conditions are shown in Fig. S1. Generally, the smaller the Nyquist semicircle diameter, the lesser the charge transfer resistance obtained at the interface between the metal surface and the electrolyte solution, which increases the corrosion rate. In addition, in the bode plot, as the resistance at low frequency increases, the corrosion inhibition increases.

Evidently, the diameters of the Nyquist plots of the bare steel is decreased with the increase in the exposure time, as shown in Fig. 2a, signifying an increase in the corrosion resistance. This is due to the formation of a porous layer from the corrosion products, which is due to the presence of high concentrations of sulphide, as proved in the literature [45,46]. It is known from the literature that the presence of low concentrations of sulphide (<500 ppm) in the electrolyte leads to the formation of a protective layer that decreases the corrosion rate of the steel. Whereas, high concentrations of sulphide (>500 ppm) form a porous layer, which is easily removed leaving the bare metal exposed to increased corrosion. By increasing the exposure time, this layer deteriorates and becomes looser after 24 h, leading to a higher corrosion rate. Fig. 2b shows the Bode/phase angle plots of the bare metal that have the same decreasing trend of its corresponding Nyquist ones. Furthermore, the smallest angle (45°) is shown with the phase angle plot of the immersed substrate for 24 h in the electrolyte.

There is a big difference in the Nyquist loop size of the bare steel and those of the deposited steel, as compared to Fig. 2 with Fig. 3 and Fig. S1. The partial FeS-deposited specimens during all the immersion times have less Nyquist semicircles compared to the bare ones, whereas those of the partial FeS_2 and SiO_2-deposited specimens have larger Nyquist loops after 6h immersion times. All full-deposited steels during the given immersion times have the same trend compared to their corresponding partial ones, except for the SiO_2 deposit. Contrary to the partial SiO_2-deposited steels, the full one has Nyquist loops higher than that of the bare metal at zero immersion times, as shown in Fig. S1. This is attributed to the chemical behaviors and the specific effect of each deposit regarding the steel's corrosion. In Fig. 3a, the size of the Nyquist loop of

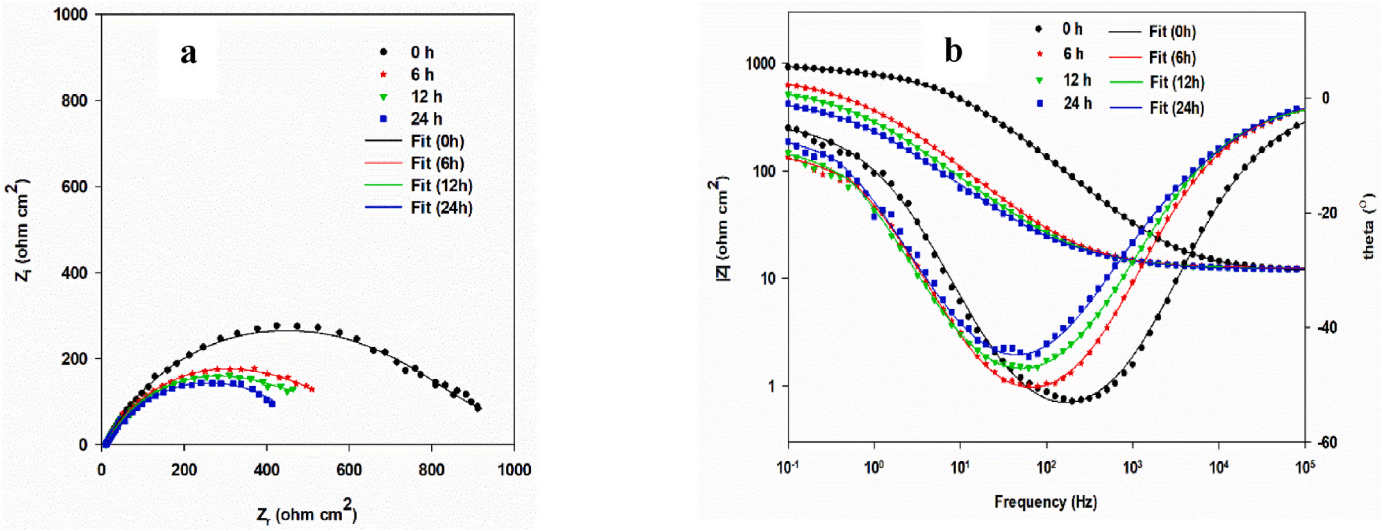

Fig. 2. a) Nyquist and b) Bode plots of the immersed bare steel in sulfated CO_2-saturated brine solution for different immersion times (0, 6, 12 and 24h) at 60 °C with 1000 rpm rotation.

the partial FeS-deposited steel increases with the immersion time from 0h to 12h but, after that, decreases at 24h. In the presence of the partial coverage of the FeS_2 or SiO_2 deposit [Fig. 3 (b and c)], the size of the Nyquist loop of the steel increases as the immersion time increases until 24h. This may be attributed to the film's morphology that is formed on the substrate by each deposit. It was noticed that FeS′ film has defects and cracks, which allows the electrolyte to diffuse through it and decreasing the protection ability with time passing, as shown in SEM photos that will be discussed later. In addition, the accumulation of conducting species into the FeS-deposit porosity that might be happened after 24h. Whereas, FeS_2 and SiO^2 have a film with higher compactness. Furthermore, for any given time considered, the Nyquist loop of the steel that is partially covered with FeS_2 has the most significant size compared to the corresponding one that is partially covered with FeS or SiO_2 deposit. Comparing Fig. 3 and Fig. S1, it is noticed that the Nyquist plots of the steel specimens fully covered with any deposits (Fig. S1) at any given time have the same trend, but still larger sizes compared to the corresponding ones that are partially covered (Fig. 3). In addition, it is worth mentioning that the Bode and the phase angle plots for the specimens that are either partially or fully covered with each deposit have the same increasing or decreasing trend as their corresponding Nyquist plots. For example, in Fig. 3a', the bode plots of the partially covered steel with FeS increase with immersion time till 12h and then decrease at 24h. Similarly, the phase angle of the partially covered steel with FeS increases with immersion time until 12h and then decreases at 24h.

Furthermore, there is an observable shift in the phase peaks of the FeS-deposited steel to the low frequencies at all given immersion times compared to the shift found in the phase peaks of SiO_2-deposited steels. This shift in the low-frequency area refers to high electrical capacitance behavior, which causes a higher corrosion rate [47]. Whereas, the phase angle θ vs. log frequency plots for the FeS_2-deposited steel do not show that shift, as shown in Fig. 3b'. This demonstrates that the FeS_2-deposited steel protects significantly against the sulfated CO_2-saturated brine solution.

The experimental EIS data for the bare, partial, and full coverage of different deposits are analyzed and fitted using the equivalent circuits (ECs) shown in Fig. 4. Echem Analyst™ software, Gamry 3000, was used for fitting the EIS outcomes. It is worth mentioning that in Nyquist EIS plots, the colored solid lines represent the fitting EIS data, and the measured ones are deployed by colored dotted symbols. Fig. 4a presents a one-time constant equivalent circuit whereas Fig. 4b and c displays two-time constants equivalent circuits without and with diffusion, respectively. R_1 and R_2 are the pore and the charge transfer resistances, respectively. The constant phase elements CPE_1 and CPE_2 are the capacitive elements associated with the pore and the charge transfer resistances, respectively. The first-time constant (R_1 CPE_1) is related to either corrosion product or deposit or both. The other time constant (R_2 CPE_2) relates to the metal/interface interaction.

Additionally, the diffusion element (W) represents the diffusion of the electrolyte to the substrate. Furthermore, n_1 and n_2 are the double-layer capacitance (C_{dl}) deviation parameters. A non-uniform corrosion reaction on the surface, surface roughness, the irregular thickness of the deposits or corrosion inhibitor or scale layers, and/or inconsistent current distribution are some reasons that lead to moving away from the ideal double layer [46]. Therefore, the CPE, composed of deviation parameters and capacitance, is used. The capacitance behavior is fundamentally ascribed to the nature of the dielectric of the film, which is formed from an inhibitor and/or corrosion product that influences the corrosion rate of the substrate and expresses by Equation (5):

$$Z_{CPE} = \frac{1}{Y_0\,(jw)^n} \tag{5}$$

where (j) is the imaginary number. *The* (Y_0) is the constant and equivalent to ($1/|Z|$) at (ω) = 1 rad/s. The (ω) is the angular frequency at the AC signal of (1/rad). The (n) is the CPE exponent. When (n) becomes 1, the CPE offers ideal behavior. Equation (6) [46,47] is utilized to estimate the double layer capacitance of the metal.

$$C_{dl} = \sqrt[n]{\frac{Y_2}{R_2^{(n-1)}}} \tag{6}$$

where Y_2 is the CPE constant for the metal and R_2 represents the charge transfer resistance (R_{ct}).

The equivalent circuit of one-time constant, which can be used for analyzing electrodes undergoing uniform corrosion, shown in Fig. 4a, is used to fit the EIS data of the bare steel. In the absence of the deposits, the bare steel displays uniform corrosion. The fitted parameters of the bare steel are shown in Table 1. It is obviously noticed that the R_1 and R_2 values decreased as the immersion time increases. Consequently, the corrosion rates increased. The enhanced values of the C_{dl} of the steel with time refer to the acceleration of the steel corrosion. The EIS data of each specimen that is either partially or fully covered with any deposits are fitted using the equivalent circuit shown in Fig. 4b, two-time constants. In addition, the diffusion element (W) appears in the two-time constants equivalent circuit shown in Fig. 4c to fit the partially

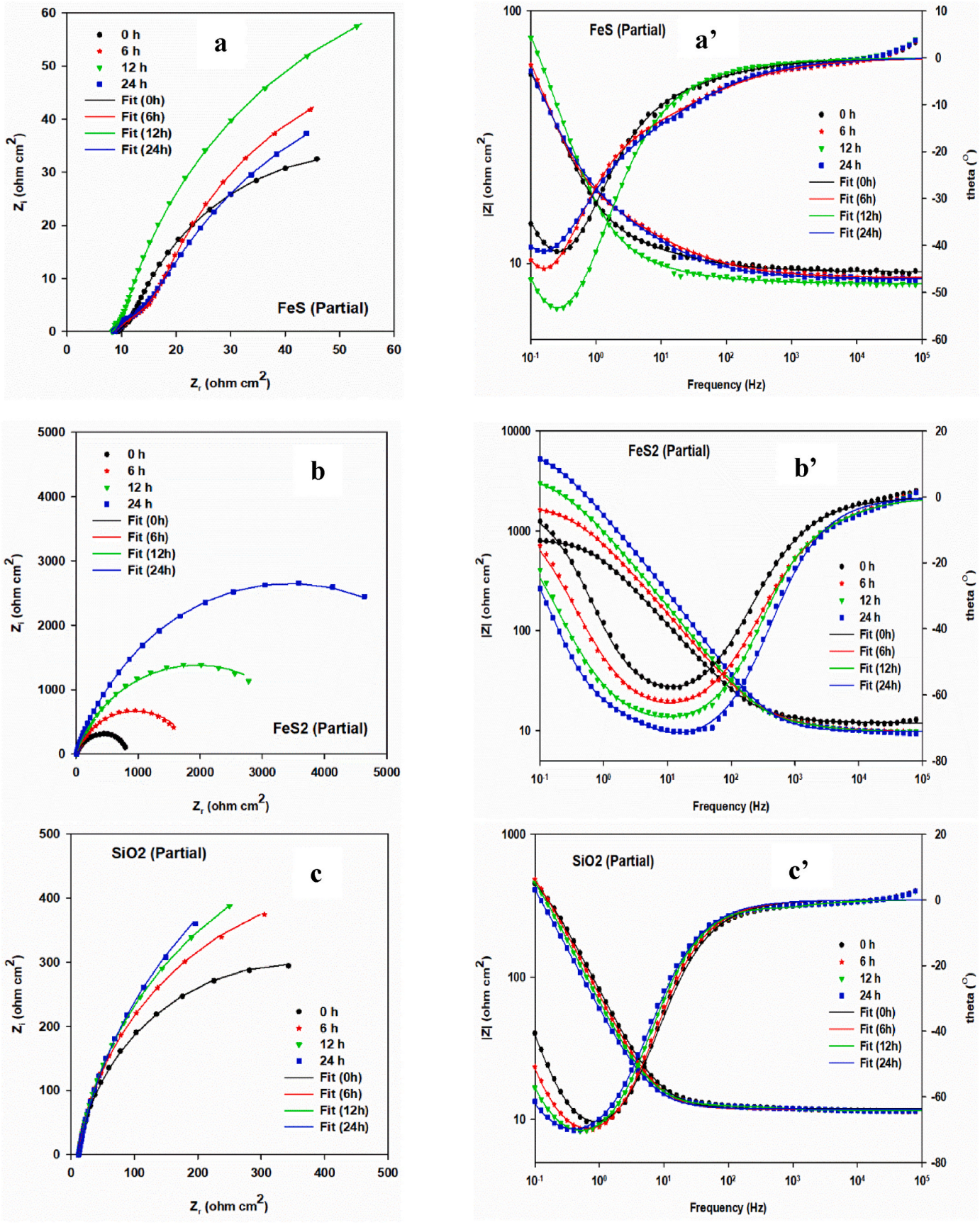

Fig. 3. Nyquist plots (a, b, and c) and their corresponding Bode plots (a', b' and c') of the uninhibited partial-deposited steel with different deposits immersed in sulfated CO_2-saturated brine solution at 60 °C with 1000 rpm rotation for different immersion times (0, 6, 12 and 24h).

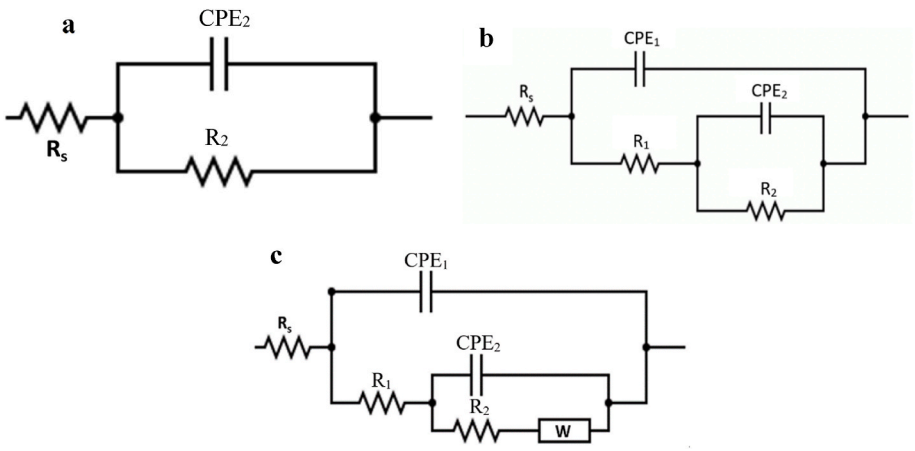

Fig. 4. Electrochemical equivalent circuits, a) one-time constant, b) two-time constants and c) two-time constants with diffusion.

Table 1
The electrochemical parameters of the obtained EIS results for the uninhibited partial-deposited steel with different deposits immersed in sulfated CO_2-saturated brine solution at 60 °C with 1000 rpm rotation for different immersion times (0, 6, 12 and 24h).

Samples' name	Time (h)	R_1 (ohm. cm^2)	CPE_1		R_2 (ohm. cm^2)	CPE_2		C_{dl} (μF. cm^{-2})	W (S.s$^{1/2}$)	Corrosion rate (mm/year)	θ	IE (%)	Goodness of fit
			Y_1 (s^n ohm^{-1} cm^{-2})	n_1		Y_2 (s^n ohm^{-1} cm^{-2})	n_2						
CS	0	–	–	–	915 ± 7.2	194 e−6 ± 1.6 e−6	0.57	52.6	–	0.330641	–	–	820.1 e−6
	6	–	–	–	586 ± 8.7	616 e−6 ± 10 e−6	0.69	389.7	–	0.517765	–	–	767.7 e−6
	12	–	–	–	499 ± 7.5	882 e−6 ± 15 e−6	0.67	588.7	–	0.608036	–	–	618.0 e−6
	24	–	–	–	397 ± 6.4	992 e−6 ± 17 e−6	0.65	600.6	–	0.764257	–	–	861.6 e−6
CS/FeS	0	3.3 ± 5 e−3	224 e−4 ± 13 e−4	0.50	83 ± 6.4	73 e−3 ± 2.4 e−3	0.85	100321	379 e−3 ± 18 e−6	3.645023	–	–	581.6 e−6
	6	9.0 ± 11 e−3	172 e−4 ± 19 e−4	0.49	121 ± 5.2	34 e−3 ± 1.7 e−3	0.88	41232	205 e−3 ± 7.5 e−6	2.500305	–	–	450.2 e−6
	12	11 ± 21 e−3	167 e−4 ± 13 e−4	0.54	160 ± 5.5	21 e−3 ± 1.5 e−3	0.82	27400	181 e−3 ± 7.0 e−6	1.890855	–	–	651.7 e−6
	24	2.9 ± 6.2 e−3	264 e−4 ± 33 e−4	0.52	111 ± 8.8	21 e−3 ± 1.6 e−3	0.92	22603	45 e−3 ± 3.8 e−6	2.725557	–	–	888.6 e−6
CS/FeS_2	0	4.3 ± 20 e−3	348 e−6 ± 13 e−7	0.70	704 ± 5.7	912 e−6 ± 14 e−6	0.89	863	–	0.429740	–	–	662.2 e−6
	6	6.9 ± 12 e−3	908 e−7 ± 68 e−7	0.77	1889 ± 12	203 e−6 ± 5.2 e−6	0.78	155	–	0.160157	0.6897	68.9	97.20 e−6
	12	11 ± 29 e−3	127 e−7 ± 13 e−7	0.77	3885 ± 32	174 e−6 ± 5.9 e−6	0.70	147	–	0.077873	0.8715	87.2	322.8 e−6
	24	108 ± 21 e−3	179 e−7 ± 30 e−7	0.78	7193 ± 56	127 e−6 ± 6.4 e−6	1.00	127	–	0.042060	0.9448	94.4	110.8 e−6
CS/SiO_2	0	140 ± 77 e−3	43 e−7 ± 11 e−8	0.91	541 ± 4.4	107 e−6 ± 5.2 e−6	1.00	107	–	0.559218	–	–	448.1 e−6
	6	364 ± 78 e−3	25 e−7 ± 2.1 e−8	0.91	894 ± 18	975 e−7 ± 14 e−8	0.99	95	–	0.338408	0.3445	34.5	865.2 e−6
	12	711 ± 83 e−3	15 e−7 ± 2.6 e−8	0.91	1140 ± 15	238 e−8 ± 2.9 e−9	0.91	1.3	–	0.265383	0.5622	56.2	2.029 e−6
	24	1399 ± 93 e−3	24 e−7 ± 2.3 e−8	0.88	1226 ± 17	221 e−8 ± 4.4 e−9	1.00	2.2	–	0.246767	0.6762	67.6	161.2 e−6

covered specimen with FeS. In addition, the phase angle curves for all deposited specimens (Fig. 3 (a', b', and c')) exhibit the two capacitance loops, and their maximum ranges from 30° to 70°, representing the different capacitance behavior of each deposit. Furthermore, as seen in Table 1, the n values varied from 0.7 to 1 for the deposited specimens, which are higher than that of bare metal. This clarified that some inhibition from the deposited samples is offered.

All fitting parameters are detailed and constructed in Table 1 and Table S1 for partial and full coverage of deposits, respectively. It is discerned that the under-deposit corrosion resistances (R_2) of the partially covered specimens in sulfated CO_2-saturated brine solution are smaller than those of the fully covered throughout all immersion times, as shown in Table 1 and Table S1, respectively. Since, in the case of partial coverage of the deposits, galvanic cells are formed along the steel surface due to the presence of steel areas covered with a deposit, which acts as an anode, and the adjacent areas without deposit, which become cathode of the galvanic cell. Therefore, the potential difference between the anodes and their cathodes leads to the formation of localized corrosion [48]. In the active oil and gas pipeline, due to the cathodic areas being significantly larger than the anodic ones, rapid corrosion occurs in the anodic areas under the deposit. This is also clarified from the corrosion rate values of the partial and full coverage of the deposits

that are noted in Table 1 and Table S1, respectively. In addition, the potential drop that takes place under the deposit and the different open circuit potentials because of the different solution chemistry at the bare and under the deposit lead to an increase in the corrosion rate of the partially covered sample.

Furthermore, despite the increase in the values of the resistances R_1 and R_2 of the FeS-covered steel (partially or fully) with immersion time, the presence of FeS accelerates the corrosion rates by about 11 and 3.6 times for the partially covered steel, and about 9.2 and 2.6 times for the fully covered one, at 0h and 24h immersion time, respectively, compared to their values in the absence of the deposits, as shown in Table 1 and Table S1. The higher corrosive effect of FeS deposit is attributed to its electronic semi-conductivity behavior, which makes it act as electrodes and contributes to the coupled charge transfer processes related to the metal corrosion in the electrolytes [49]. As proved in the literature [50], FeS presents six modifications in nature. These various modifications are transformed electrochemically in the corrosion potential range of the iron [21]. The sulfide can be oxidized to thiosulfate or elemental sulfur, which are very electroactive [51,52], by the oxygen traces present in the electrolyte. At the same time, the sulfur can be reduced to sulfides and thiosulfate on the FeS deposit and the metal surface to activate the sulfur compounds. Moreover, it is proved in the literature that the used commercial FeS powder that acts as a deposit is extensively oxidized, leading to various intermediate sulfur products that introduce extra corrosion effects [53]. In addition, the highest C_{dl} values of the FeS-deposited specimens throughout the immersion times compared to those of the FeS_2 and SiO_2-deposited and the deposit-free specimens reflecting the higher corrosion properties of the FeS-deposited samples. Furthermore, the appearance of the "*W*" element, which is decreased with the immersion time clarified the easy penetration of the electrolyte into the FeS-deposited samples with the time.

On the contrary, the presence of FeS_2 and SiO_2 deposits in partial or full coverage on the steel increases the values of R_1 and R_2, and diminishes the corrosion rates of the bare steel with the immersion time, as shown in Table 1 and Table S1. In the case of partial coverage of FeS_2 and SiO_2, the corrosion rates of the bare metal are decreased by about 18.2 and 3.1 times, respectively, after 24h passed in the electrolyte. At that time, the inhibition efficiencies of these deposits reach 94.4 % and 67.6 %, respectively, as shown in Table 1. On the other hand, the inhibition efficiencies of the FeS_2 and SiO_2, when they fully cover the steel, become about 96.5 % and 90.1 % (Table S1), respectively, after an immersion time of 24h. This relates to a surface coverage and mass transfer effects combination [54]. Since the available surface area for corrosion is reduced by the deposits. Therefore, the diffusion of the corrosive species to the steel surface is restricted.

Moreover, the decreasing trend of the CPE_1, CPE_2 and C_{dl} of the FeS_2 and SiO_2-deposited samples refers to the inhibition behavior of these deposits. Noticeably, the FeS_2 has the highest resistances and lowest corrosion rates throughout the mentioned immersion times compared to the other two deposits. The smallest particle size, about 44 μ, of FeS_2 may be the possible reason that impedes the electrolyte from reaching the metal and help in the temporary corrosion inhibition underneath. In addition, the formation of corrosion products is another considerable factor affecting the corrosion processes [55]. Iron carbonate ($FeCO_3$) is the essential corrosion product for carbon steel in the CO_2-saturated brine solution. More corrosion products like hydroxides ($Fe(OH)_2$), oxyhydroxides (FeOOH), iron oxides (Fe_3O_4), and hydroxycarbonates ($Fe_2(OH)_2CO_3$) can also form [56,57].

It is known that the sand is electrochemically inactive. Generally, it is proved in the literature that the existence of inert or non-conductive deposits, like sand, acts as a diffusion barrier against the mass transfer of the corrosive species or any oilfield chemicals present. Therefore, the inert deposits retard the corrosion that may take place under it [13]. Despite the inert behavior of the sand, its inhibition efficiencies along the given immersion times are lower than those of FeS_2. This can be attributed to the utilized SiO_2, which has a bigger particle size (62 μ) compared to FeS_2; it will be later clarified in the characterization section. Moreover, the increase of the R_1 and R_2 values of the partial SiO_2-deposited specimens with time may be attributed to the rise of the corrosion products within the sand deposit by blocking the places where the metal starts to lose or occurring the cathodic reactions. This is in parallel with the literature [58].

As it is previously mentioned, the impact of deposits on UDC primarily depends on their composition, density (porosity), and extent of coverage. These factors are usually interconnected, making it difficult to isolate their individual effects on UDC [59]. Regarding the sand deposits, some investigations coincide with our results and have reported protective effects of sand deposits on UDC [13,60,61]. However, other investigations proved that sand can promote both uniform and localized corrosion due to its porosity [62–64]. There have been relatively few studies on UDC under iron sulfide deposits, likely due to the challenge of performing UDC tests on semiconductive materials [59]. The limited research available suggests that mackinawite deposits, which are relatively porous and offer poor protection, can induce UDC [65]. In contrast, UDC under pyrrhotite or troilite deposits is less severe due to their higher compactness [65–67].

3.1.2. The performance of the inhibitor (CR11) in the absence of deposits

Fig. 5 (a and b) shows the Nyquist plots and their corresponding Bode plots of the EIS results for J55 steel in sulfated CO_2-saturated brine solution in the presence of different concentrations (5, 10, 25, 50, 100, 200, 300, 400, and 500 ppm) of CR11. The EIS experiments are done under the same previous condition: high flow conditions (rotation at 1000 rpm) and high temperature (60 °C). As shown in Figs. 2 and 5, it is noticed that the Nyquist plots of the steel in the presence of the different concentrations of CR11 (Fig. 5a) have bigger semicircle diameters compared to that of the bare steel throughout all immersion times (Fig. 2a). This clarifies the inhibitive effect of the inhibitor that comes from the presence of the amine group, as it is amine salt of organic phosphates, as described in its datasheet. This indicates the easy diffusion of the inhibitor to the steel surface through the porous iron sulfide and iron carbonates layer formed on the steel because of the anodic and cathodic reactions of the iron in the acidic solution containing CO_2 and H_2S, as seen in the following equations.

In the case of H_2S,

$$H_2S \rightarrow H^+ \text{ (reduction of } H_2S) \quad (7)$$

$$2H^+ + 2e^- \rightarrow H_2 \text{ (reduction of } H_2) \quad (8)$$

$$Fe \rightarrow Fe^{2+} + 2e^- \text{ (oxidation of Fe)} \quad (9)$$

$$S^{2-} + Fe^{2+} \rightarrow FeS \text{ (precipitation of FeS)} \quad (10)$$

In the case of CO_2,

$$H_2CO_3 + 2e^- \rightarrow H^+ + HCO_3^- \text{ (reduction of } H_2CO_3) \quad (11)$$

$$2HCO_3^- \rightarrow 2H+ + 2CO_3^- \quad (12)$$

$$Fe^{2+} + CO_3^- \rightarrow FeCO_3 \text{ (precipitation of } FeCO_3) \quad (13)$$

Comparing the Nyquist plots of the inhibited steel (Fig. 5a), it is illustrated that the semicircle diameters of the inhibited steel are increased as the inhibitor concentration in the electrolyte is increased, and the widest one is observed at 400 ppm of CR11. This indicates that the optimum concentration of CR11 is at 400 ppm, at which the resistance of the J55 steel is the highest compared to the other concentrations. The Bode plots shown in Fig. 5b display the same trend as their corresponding Nyquist ones. In addition, the phase angle plot of the inhibited steel with 400 ppm inhibitor has the largest angle, which is 78°.

The EIS data of the inhibited steel in the presence of different concentrations of CR11 is fitted using the equivalent circuit represented in

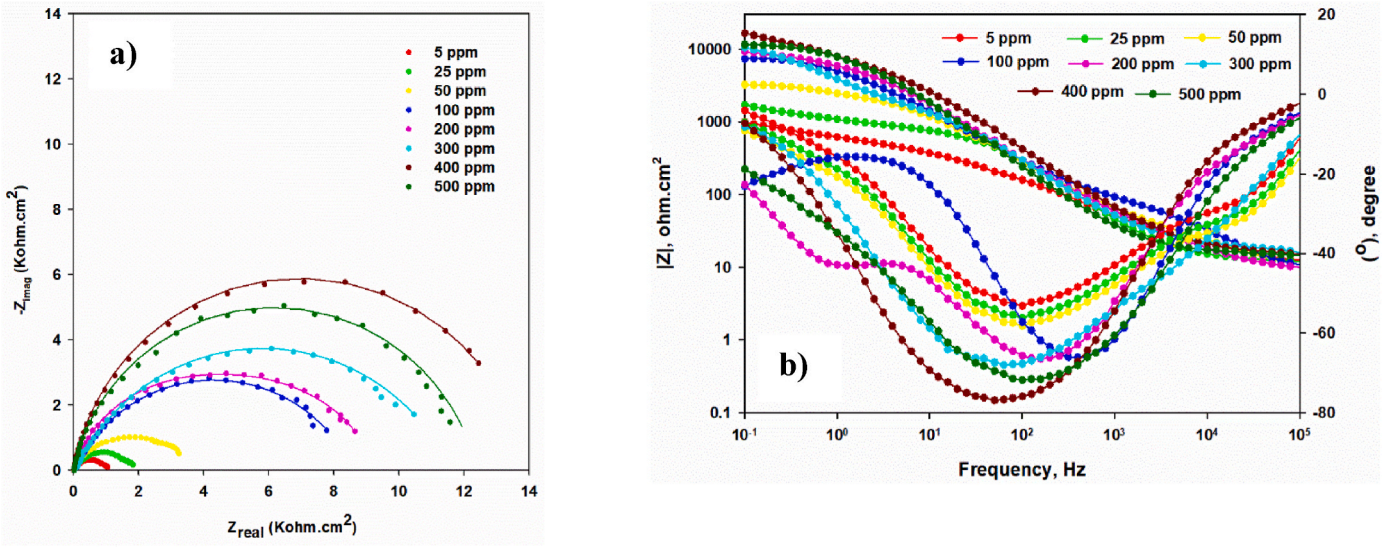

Fig. 5. a) Nyquist plots and b) Bode-phase angle plots of the J55 steel in the presence of different concentrations of CR11 in sulfate CO_2-saturated brine electrolyte (3.5 wt% NaCl + 1000 ppm Na_2S + CO_2 purging) at a rotation of 1000 rpm and 60 °C. The exposure time for achieving EIS is 30 min.

Fig. 4b, which is two-time constants. This circuit mostly uses electrodes with coatings or adsorbed layers on top [68–70]. The R_2 values of the inhibited steel increase with increasing the inhibitor concentration until the optimum one, which is 400 ppm. After that concentration, the R_2 value is decreased. Therefore, 400 ppm of CR11 increases the R_2 value of the inhibited steel about 19.85 times compared to its resistance in the absence of the inhibitor (R_2 of the substrate at 0h). It is worth mentioning that the R_1 values of the inhibited steel have the same trend as the R_2 ones, as shown in Table 2, and the highest value of the R_1 is noticed at a concentration of 400 ppm. Moreover, the inhibition efficiencies of the inhibited steel are increased as the inhibitor concentration is increased, reaching the maximum of about 95 % at 400 ppm.

Based on Uhlig and Bohni [71], the formation of a passive film that is stimulated by the existence of the inhibitor molecules, which block the active site on the steel surface, can explain the increasing charge transfer resistance values (R_2). Another explanation can be the higher amounts of adsorbed layer area and/or thickness of the inhibitor that works as a physical obstacle. This is proved by the decrease of C_{dl} values, as shown in Table 2, which clarifies the increase in the thickness of the electrical double layer that reflected the adsorption of the inhibitor molecules instead of water molecules on the metal surface. Equation (14) is expressed as the double layer capacitance (C_{dl}), which is explained according to the Helmholtz model [72,73].

$$C_{dl} = \frac{\varepsilon\, \varepsilon^{o}}{d} A \tag{14}$$

where ε is the medium dielectric constant, ε^{o} is the permittivity of the vacuum, A is the surface area of the electrode, and d is the protective layer thickness.

In addition, it is noted that the least C_{dl} value is observed at concentration of 400 ppm. Furthermore, the n values are lower than that of bare metal, and vary from 0.77 to 0.95, having the highest value at 400 ppm concentration of CR11. This proves that the inhibitor has outstanding inhibition properties, with the optimum concentration at 400 ppm.

Therefore, the inhibition efficiencies, *I.E.* %, and the surface coverage, θ, of the CR11 inhibitor increase as the inhibitor concentration increases. Consequently, the corrosion rate decreased until reaching its optimum concentration. Then, it starts to diminish, and the corrosion rate increases due to the diffusion of the Cl^- ions, which breaks down the protective layer and leads to a localized attack on the metal. The surface coverage of the inhibitor, its corrosion rates, and its inhibition efficiency

Table 2
EIS parameters obtained for the J55 steel in the presence of different concentrations of CR11 in the electrolyte (3.5 wt % NaCl +1000 ppm Na_2S + CO_2 purging) at a rotation of 1000 rpm and 60 °C.

Samples' name	C_{inh} (ppm)	R_1 (ohm. cm^2)	CPE_1		R_2 (ohm. cm^2)	CPE_2		C_{dl} (μF. cm^{-2})	Corrosion rate (mm/year)	θ	*IF* (%)	Goodness of fit
			Y_{o1} (s^n ohm^{-1} cm^{-2})	n		Y_{o2} x 10^{-6} (s^n ohm^{-1} cm^{-2})	n					
CR11	5	605 ± 7.1	130 e−6 ± 8.1 e−6	0.55	1195 ± 16	30.8 e−6 ± 2.1 e−6	0.67	6.05	0.253169	0.234	23.4	945.0 e−6
	25	547 ± 3.0	67.6 e−6 ± 1.6 e−6	0.79	2720 ± 23	17.5 e−6 ± 1.1 e−6	0.70	4.75	0.111227	0.663	66.3	264.9 e−6
	50	617 ± 8.4	66.6 e−6 ± 1.4 e−6	0.88	3780 ± 31	21.6 e−6 ± 2.9 e−6	0.77	10.2	0.080036	0.758	75.8	1.367 e−6
	100	998 ± 17	45.0 e−6 ± 1.3 e−6	0.72	8430 ± 110	15.0 e−6 ± 1.6 e−6	0.90	11.9	0.035888	0.891	89.1	319.8 e−6
	200	1000 ± 21	22.3 e−6 ± 2.6 e−6	0.80	9900 ± 230	12.7 e−6 ± 3.1 e−6	0.95	11.4	0.030559	0.908	90.8	983.6 e−6
	300	1198 ± 19	22.0 e−6 ± 2.8 e−6	0.99	11800 ± 454	13.5 e−6 ± 1.3 e−6	0.89	10.7	0.025639	0.922	92.2	6.546 e−6
	400	1570 ± 18	12.8 e−6 ± 3.2 e−6	0.99	18170 ± 691	2.2 e−6 ± 4.8 e−9	0.96	1.91	0.018710	0.949	94.9	1.689 e−6
	500	1450 ± 20	48.5 e−6 ± 4.1 e−6	0.86	12660 ± 355	4.7 e−6 ± 2.8 e−9	0.84	2.74	0.023897	0.928	92.8	1.187 e−6

values are displayed in Table 2.

By comparing the resistivity and the corrosion rate, as represented in Table 2, of the inhibited J55 steel in the presence of different concentrations of the inhibitor, it is noticed that the inhibitor has specific stability behavior. Therefore, the concept of "addition of more commercial of inhibitor is better" will not be true now.

3.1.3. *The performance of CR11 in the presence of the different deposits for different immersion times*

In this section, the influence of the partial and full coverage of the different deposits on the effectiveness of the CR11 is evaluated in the sulfated CO_2-saturated brine solution under the same previous conditions (at 60 °C with 1000 rpm rotation) for different times (0, 6, 12 and 24h). The optimum concentration of CR11 (400 ppm) is chosen for this

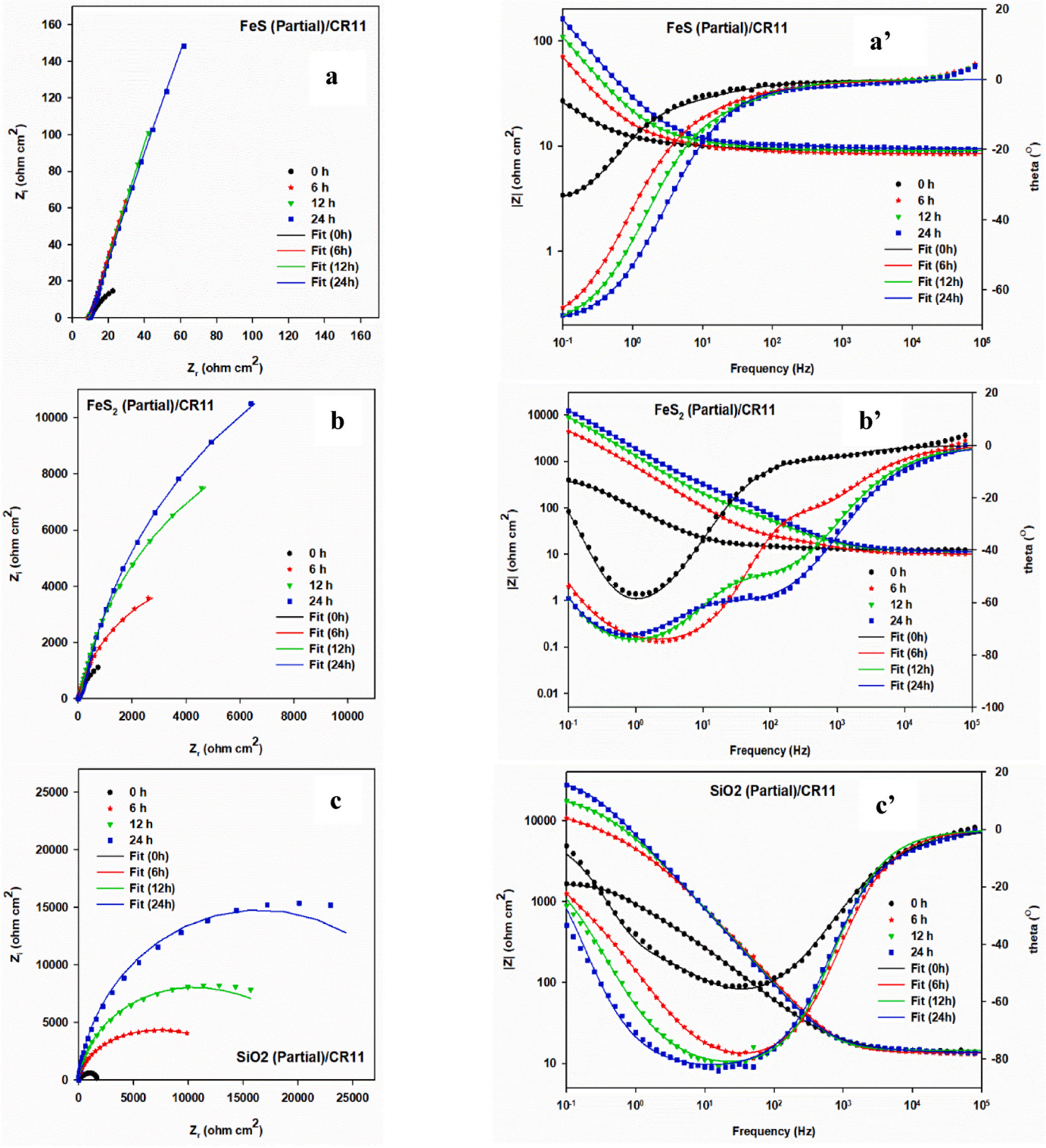

Fig. 6. Nyquist plots (a, b, and c) and their corresponding Bode plots (a', b', and c') of the inhibited partial-deposited steel with different deposits immersed in the sulfated CO_2-saturated brine solution at 60 °C with 1000 rpm rotation for other times (0, 6, 12, and 24h).

test. Fig. 6 shows the Nyquist plots (a, b, and c) and their corresponding Bode plots (a', b', and c') of the EIS results for the inhibited partial-covered steel specimens with FeS, FeS_2, and SiO_2, respectively. Fig. S2 represents the EIS results for the corresponding inhibited full-covered steel specimens.

It is well noticed that the Nyquist semicircle diameters for the partial and full-covered specimens with all different deposits in the inhibited electrolyte solution increase as the immersion time increases, as shown in Fig. 6 and Fig. S2. This is attributed to the inhibitor's effectiveness that enhanced with time due to its gradual transportation through the deposits reaching the substrate sites beneath them. Moreover, at the beginning of the immersion time until 6h, the Nyquist semicircle diameters for the inhibited FeS and FeS_2, either partial or full-covered samples (Fig. 6 (a, b) and S2 (a, b)), are lesser than that one of the corresponding bare metal (Fig. 2a). After that, they became higher than those of bare metals at the corresponding immersion time. This indicates the beginning slow diffusion of the inhibitor through FeS and FeS_2 deposits into the substrate. Commonly, the adsorption of the inhibitor over the deposit surface is supposed to decrease with the deposit with a large particle size (or smaller specific surface area) [74]. As in Table S3, FeS and FeS_2 have smaller surface areas than SiO_2. However, the Nyquist semicircle diameters for the inhibited FeS and FeS_2, either partial or full-covered samples (Fig. 6 (a, b) and S2 (a, b)), are higher than those of the corresponding uninhibited FeS and FeS_2 either partial or full-covered samples (Fig. 3 (a, b) and S1 (a, b)) at all immersion times, indicating the inhibitor action. Whereas the Nyquist semicircle diameters for the inhibited SiO_2, either partial or full-covered samples (Fig. 6c and Fig. S2c) are higher than that of the bare metal (Fig. 2a) and the corresponding uninhibited ones (Fig. 3c and Fig. S1c) along all given immersion times.

Furthermore, it is noted that the Nyquist semicircle diameters for the inhibited SiO_2, either partial or full-covered samples (Fig. 6c and Fig. S2c) are higher compared to their corresponding FeS and FeS_2-covered illustrations (Fig. 6 (a, b) and S2 (a, b). This indicates the inactive behavior of SiO_2 and its good compatibility with the inhibitor. In addition, based on the physical measurements of the deposits shown in Table S3, SiO_2 has an enormous pore volume compared to FeS and FeS_2, which permits and facilitates the inhibitor to diffuse into the substrate in large amounts and inhibits the substrate's area under deposit as well. Therefore, it is worth mentioning that the efficiency of the inhibitor is affected by the presence of the deposit, its type, its porosity, and its compatibility with the inhibitor [75]. The bode plots for all inhibited partial or complete covered samples with all different deposits have the same increasing and decreasing trend compared to the corresponding Nyquist ones, as shown in Fig. 6 and Fig. S2, respectively. In addition, all inhibited deposits partially covered by the substrate have higher Nyquist semicircle diameters than their corresponding full ones. This is expected for the partial coverage samples due to the diffusion of the inhibitor into the substrate and the formation of the protective film over its naked areas, in addition to the barrier effects of the deposits that inhibit the distribution of the corrosive ions. It is observed that the Nyquist semicircle diameter for the inhibited full or partial covered specimens with all deposits after 24h immersion time has the following order, $SiO_2 > FeS_2 > FeS$. In contrast, that of the uninhibited full or partially covered specimens is as follows $FeS_2 > SiO_2 > FeS$. This can be due to the more diminutive compatibility of FeS_2 with the inhibitor compared to the SiO_2 and its lower pore volume.

Table 3 and Table S2 illustrate the calculated parameters from the equivalent circuits shown in Fig. 4 (b and c). They fitted the impedance data to two-time constants without and with diffusion for both partial and complete coverage deposits on the steel. In Table 3 and Table S2, it is elucidated that the UDC resistance (R_2) for all inhibited deposited samples increases with immersion time. In addition, the R_2 for the inhibited partial/full FeS-deposited specimens is larger than the corresponding uninhibited partial/full FeS-deposited specimens for all times, reaching a maximum increase of 94.3 and 34 times after 24 h for partial and full coverage, respectively, as shown in Tables 1, 3, Tables S1 and S2. This indicates that the inhibitor can pass through the FeS reaching the substrate, and providing satisfactory inhibition despite the higher conductivity of the FeS that causes corrosion acceleration in the absence of the inhibitor. This may be due to the large pore volume of the FeS, the porous nature of the deposit and the acceptable compatibility with the inhibitor. In addition, similar to the inhibited FeS-deposited specimens, the inhibited FeS_2- and SiO_2-deposited (either partial or full) specimens show enhanced values of R_2 compared to the corresponding uninhibited deposited specimens. For example, the R_2 of the inhibited partial/full FeS_2-covered sample shows 3.57 and 1.04 times increase compared to the corresponding uninhibited ones after 24 h. Whereas, the inhibited partial/full SiO_2-covered samples offer about 26.92 and 3.86 times increase in the R_2 compared to the corresponding uninhibited ones after 24 h. This clarifies the explicit compatibility of the inhibitor with the FeS, which offers the highest increase in the resistivity difference between its inhibited and uninhibited samples. Based on the previous increase in the resistivity difference between the uninhibited and inhibited samples of the different deposits, the order of the compatibility of the inhibitor with them is as follow: $FeS > SiO_2 > FeS_2$. The least compatible with the inhibitor is FeS_2 due to its high compactness that impedes the diffusion of the inhibitor. Despite the moderate compatibility of SiO_2 with the inhibitor, it shows the highest inhibition efficiencies throughout the whole immersion time. Therefore, it is worth mentioning that the presence of deposits and its way of coverage on the steel influenced the inhibitor passage and its accessibility at the steel surface, impeding the inhibitor from being effective at the steel underneath. Generally, the pore resistance of the deposits (R_1) for all the inhibited deposited specimens, either partially or fully covered by the substrate, has the same trend as the corresponding R_2. There is a good fit between the experimental data and the equivalent circuits modeling over the measurement frequency range.

The coming section is the characterization of these stages concerning the corrosion mechanism of the different specimens.

As seen in Table 4, it is worth mentioning that most organic inhibitors that contain N, O, and P heteroatoms, especially imidazoline and its derivatives have UDC inhibition efficiencies below 70 % [76–78]. Interestingly, many S-containing compounds exhibit excellent UDC inhibition effectiveness, with over 90 % efficiency [79,80]. However, not all S-containing compounds are effective UDC inhibitors, such as thiourea-based alkyl imidazoline under mixed deposits [81]. Pang et al. [82] recently discovered the ideal design strategy for a UDC inhibitor, confirming that it must fulfill three conditions: (1) exhibit some degree of corrosion inhibition for bare metal, (2) be able to easily penetrate through deposits to reach the metal surface, and (3) have a low propensity for adsorption on deposits. Consequently, the used inhibitor satisfies all three conditions. It has a satisfactory inhibition performance for the bare metal (95 % at 400 ppm) through adsorption, as shown in Table 2. In addition, the inhibitor penetrates the deposit seen from its inhibition effect on the electrodes partially and completely loaded with the different deposits, as clarified in Table 3 and Table S2. In addition, it is slightly adsorbed on some deposits (FeS and SiO_2). Comparing Table 1 with 3 and S1 with S2, there is a large difference in the inhibition efficiency values of the deposits before and after the addition of the inhibitor, depending on the deposit's type. This clarifies the high penetration of the inhibitor through these deposits and its low tendency to adsorb on them. Furthermore, the inspected inhibitor offered a satisfactory inhibition efficiency in sweet and sour environment, as compared to the previous inhibitors issued in the literature, as shown in Table 4.

3.2. Deposit characterization

3.2.1. Scanning electron microscope (SEM) and energy dispersive X-ray analysis (EDX)

Fig. 7 (a, b, and c, respectively) shows the SEM photos of the FeS-,

Table 3
EIS parameters obtained for the inhibited partial-deposited steel with different deposits immersed in the sulfated CO_2-saturated brine solution at 60 °C with 1000 rpm rotation for other times (0, 6, 12, and 24h). The concentration of CR11 is 400 ppm.

Samples' name	Time (h)	R_1 (ohm. cm^2)	CPE_1		R_2 (ohm. cm^2)	CPE_2		C_{dl} (μF. cm^{-2})	W $S.s^{1/2}$	Corrosion rate (mm/year)	θ	IE (%)	Goodness of fit
			Y_1 (s^n ohm^{-1} cm^{-2})	n_1		Y_2 (s^n ohm^{-1} cm^{-2})	n_2						
CS/FeS/CR11	0	2.5 ± 10 e−3	46.8 e−3 ± 46 e−6	0.78	250 ± 2.2	76.6 e−3 ± 46 e−6	0.82	146447	32.7 e−3 ± 4 e−6	1.21013	–	–	430.6 e−6
	6	5.5 ± 64 e−3	7.76 e−3 ± 11 e−6	0.68	2600 ± 29	30.5 e−3 ± 11 e−6	0.82	79655	26.4 e−3 ± 6 e−6	0.11636	0.7746	77.5	542.2 e−6
	12	6.9 ± 75 e−3	6.66 e−3± 28 e−6	0.67	3300 ± 31	25.1 e−3 ± 19 e−6	0.88	45840	6.10 e−3 ± 8 e−6	0.09168	0.8487	84.9	564.7 e−6
	24	9.2 ± 77 e−3	5.34 e−3± 4.9 e−6	0.71	10470 ± 120	17.7 e−3 ± 6.3 e−6	0.88	36077	1.20 e−3 ± 1 e−6	0.02889	0.9621	96.2	368.0 e−6
CS/FeS_2/CR11	0	5.5 ± 22 e−3	427 e−3± 465 e−6	0.75	652 ± 11	555 e−3 ± 524 e−6	0.93	864712	–	0.46401	–	–	175.7 e−6
	6	21.4 ± 25 e−3	146 e−3± 316 e−6	0.79	10580 ± 83	255 e−3 ± 331 e−6	0.93	462157	–	0.02859	0.9446	94.5	492.6 e−6
	12	75.4 ± 37 e−3	148 e−3± 234 e−6	0.89	20810 ± 220	235 e−3 ± 251 e−6	0.92	491904	–	0.01454	0.9760	97.6	321.0 e−6
	24	185 ± 28 e−3	107 e−3± 210 e−6	0.89	25680 ± 390	124 e−3 ± 220 e−6	0.91	275343	–	0.01179	0.9845	98.5	14.49 e−6
CS/SiO_2/CR11	0	554 ± 80 e−3	195 e−3± 174 e−6	0.72	3115 ± 28	158 e−3 ± 173 e−6	0.95	218951	–	0.09712	0.7063	70.6	315.4 e−6
	6	810 ± 20 e−3	25 e−3± 36 e−6	0.57	10910 ± 72	95 e−3 ± 41 e−6	0.93	160214	–	0.02773	0.9463	94.6	1.469 e−6
	12	844 ± 22 e−3	23 e−3± 6.8 e−6	0.72	29200 ± 448	22 e−3 ± 2.2 e−6	0.95	30917	–	0.01036	0.9829	98.3	1.800 e−6
	24	953 ± 65 e−3	7.1 e−3± 7.3 e−6	1.00	33000 ± 500	19 e−3 ± 1.6 e−6	0.95	26667	–	0.00917	0.9879	98.8	1.241 e−6

FeS_2- and SiO_2-covered steel samples before immersion in the electrolyte. It is illustrated that each deposit has a distinct morphology. Noticeable cracks can be observed on the FeS-covered sample (Fig. 7a). In contrast, the FeS_2 deposit formed a compact layer on the substrate without defects (Fig. 7b), and micro-pores exist in the SiO_2-covered layer (Fig. 7c).

SEM images shown in Fig. 8 show the surface morphology of the bare steel (non-covered) and the different deposits-covered specimens after 24 h of immersion in the non-inhibited (a, b, c, and d) and inhibited (a', b', c', and d') electrolyte. The surface constituents for each specimen are investigated using EDX and shown in Table 5. Comparing the non-inhibited and inhibited specimens, the porous surface layer with different porosity and irregularity degrees depending on the type of deposit is observed on the non-inhibited specimens, as shown in Fig. 8 (a, b, c and d). On the other hand, as shown in Fig. 8 (a', b', c', and d'), the inhibited specimens show a dense and smooth film formation. At the deposits-free surface (Fig. 8a), there is no localized attack, clarifying that the uniform corrosion performs over the whole surface. This corrosion is remarkably suppressed in the presence of CR11 (Fig. 8a'), which is appeared like longitudinal dense foggy layers.

Moreover, the quantitative EDX analysis of the non-inhibited steel surface displays the peaks of Fe, C, S, and O in its spectra shown in Table 5, indicating the formation of the corrosion products because of corrosion reactions, as previously discussed. Whereas the appearance of the N and P peaks in the EDX analysis of the inhibited steel surface shown in Table 5 proves the excellent adsorption of the inhibitor on the bare metal. The C, S, and O peaks are also observed in the EDX spectra of the inhibited steel in a higher percentage than those in the non-inhibited sample. This indicates fewer corrosion products due to the good presence of the inhibitor on the steel surface resulting in an excellent resistant surface against both general and localized corrosion.

At the FeS-deposited specimens (Fig. 8b) surface, interconnected continuous porous structure is investigated, proposing more considerable metal dissolution than the deposits-free sample (Fig. 8a). Since the steel area beneath the deposit is exposed to different microenvironments, the localized attack is seen on the FeS-covered steel surface [75]. In addition, both non-inhibited and inhibited surfaces' SEM micrographs display the formation of pits, which are fewer and smaller at the inhibited surface (Fig. 8b') compared to those at the non-inhibited surface due to the inhibitor effect. Moreover, the noticeable coverage of both the non-inhibited and the inhibited specimens with cubic crystalline corrosion products proves the metal dissolution of the inhibited FeS-covered steel specimen more than the inhibited deposit-free one. This is due to the higher conductivity of FeS and the localized corrosion that happens under the deposit by accelerating the cathodic reaction of the corrosion process [75]. This is also supported by the EDX measurement (Table 5) that demonstrated the adsorption of the inhibitor at the steel regardless of the presence of the FeS deposit by the appearance of the peaks of N and P. However, it also clarified the decrease in the weight percent of the N, P, C, O, and S elements in the inhibited FeS-covered sample compared to the inhibited deposit-free one, showing the decreased inhibitor quantity that is diffused to reach the area beneath the deposit. In addition, the increased weight percent of C, O, and S in the non-inhibited FeS-covered steel sample compared to the non-inhibited deposit-free one reflects the high corrosion activity. The high corrosion rate of the inhibited FeS-covered steel acquired from the EIS measurements correlates well with the SEM/EDX analysis, which also shows that despite the presence of the CR11, localized corrosion still occurs.

On the other hand, when fine-sized FeS_2 (44 μm) and SiO_2 (62 μm) are used, a general corrosion morphology is noticed combined with small-sized defects, compared to the FeS-covered specimen, distributed over the whole non-inhibited FeS_2- and SiO_2-covered specimens surface, as shown in Fig. 8 (c and d). However, the FeS_2-covered specimens (Fig. 8c) surface shows clear observable thick film, which supports its better inhibition. The formation of such a thick film refers to the participation of more sulfur quantities, which comes from the sulfur-rich pyrite (FeS_2), in the reaction, as confirmed by EDX, which clarifies the increase of sulfur wt. % in FeS_2 compared to that in FeS. In addition, it is well known in the literature that the solubility product of pyrite (16.4 ± 1.2) is higher than that of pyrrhotite (5.1 ± 0.1) and troilite (5.25 ± 0.2) [87]. Contrariwise, in the presence of the inhibitor, the reverse pattern is seen such that the SEM image of the SiO_2-covered specimen's surface exhibits more compactness than that of the FeS_2-covered specimen one,

Table 4
The inhibition efficiencies of some selected UDC inhibitors for steel in the presence and absence of deposits in sweet and/or sour environments.

Inhibitor Name	Environment Solution Condition	Steel Type	Deposit	Conc. of Inhibitor	Inhibition Efficiency	Ref.
Amine salt of organic phosphates, including mercapto-2-methylimidazole	3.5 wt% NaCl + saturated CO_2 + 1000 ppm Na_2S at 60 °C and 1000 rpm	J55	FeS	400 ppm	0–96 % @ 0–24h immersion time	This work
			FeS_2	400 ppm	0–98.5 @ 0–24h immersion time	
			SiO_2	400 ppm	70.6–98.8 @ 0–24h immersion time	
Fatty acid imidazoline	Brine solution CO_2-saturated, 48 °C	X65	Sludge deposits	300 mg/L	53 %	[76]
Imidazoline derivative	Brine solution CO_2-saturated, 40 °C	Pipeline	Sand	25 mg/L	47.74	[77]
		Pipeline	Sand	40 mg/L	62.44	
Quaternary amine derivative	Brine solution CO_2-saturated, 40 °C	Pipeline	Sand	25 mg/L	29.44	
		Pipeline	Sand	40 mg/L	59.39	
Oleic acid imidazoline	3.5 wt% NaCl CO_2-saturated, 25 °C	Q235	$CaSiO_3$ + $MgCO_3$ + $CaSO_4$ + water	200 mg/L	53.4 %	[78]
Thiourea oleic acid imidazoline quaternary ammonium salt	3.5 wt% NaCl, 25 °C	Q235	$CaSiO_3$ + $MgCO_3$ + $CaSO_4$ + water	200 mg/L	87.03 %	
Thiourea oleic acid imidazoline	3.5 wt% NaCl, 25 °C	Q235	$CaSiO_3$ + $MgCO_3$ + $CaSO_4$ + water	200 mg/L	91.92 %	
2-mercaptopyrimidine	3 wt% NaCl +0.01 wt% $NaHCO_3$, CO_2-saturated, 30 °C	1030	SiO_2	100 mg/L	96.6 %	[79]
Thiobenzamide		1030	SiO_2	100 mg/L	95.2 %	
2-Dodecylpiridinium chloride hydrate		1030	SiO_2	100 mg/L	52.7 %	
2-mercaptopyrimidine	3 wt% NaCl +0.01 wt% $NaHCO_3$, CO_2-saturated, 30 °C	1030	Al_2O_3	100 mg/L	98.24 %	[80]
		1030	SiO_2	100 mg/L	95.02 %	
		1030	$CaCO_3$	100 mg/L	90.62 %	
2-Dodecylpiridinium chloride hydrate	3 wt% NaCl +0.01 wt% $NaHCO_3$, CO_2-saturated, 30 °C	1030	Al_2O_3	100 mg/L	3.89 %	
		1030	SiO_2	100 mg/L	3.66 %	
		1030	$CaCO_3$	100 mg/L	38.42 %	
Thiourea-based alkyl Imidazoline	Brine solution CO_2-saturated, 25 °C	X65	FeS + S + Sand + clay + $FeCO_3$	1000 mg/L	−297 %	[81]
2-mercaptobenzimidazole	3.5 wt% NaCl CO_2-saturated, 40 °C	1020	SiO_2	100 mg/L	94.67 %	[82]
		1020	$CaCO_3$	100 mg/L	98.17 %	
2-hydroxybenzimidazole	3.5 wt% NaCl CO_2-saturated, 40 °C	1020	SiO_2	100 mg/L	44.78 %	
		1020	$CaCO_3$	100 mg/L	51.19 %	
2-aminobenzimidazole	3.5 wt% NaCl CO_2-saturated, 40 °C	1020	SiO_2	100 mg/L	89.33 %	
		1020	$CaCO_3$	100 mg/L	92.45 %	
Amine salt of organic phosphates, including mercapto-2-methylimidazole	3.5 wt% NaCl + saturated CO_2 + 1000 ppm Na_2S at 60 °C and 1000 rpm	J55	–	400 ppm	95 %	This work
Three novel sulphonamides based cationic surfactants (C8, C10 and C12)	3.5 wt% NaCl + Saturated CO_2	1018	–	3×10^{-6} - 5×10^{-4} M	59.1–94.5 @ C8 63.2–97.6 @ C10 63.2–99.5 @ C12	[83]
1–benzylimidazole	CO_2-saturated 3.5 % NaCl + 100 ppm H_2S solution	C1018	–	50–200 ppm	38.95–60.38 % 80 % @ 150 ppm	[84]
Hydroxyethyl-imidazoline	3 wt% NaCl + H_2S at 50 °C	Carbon steel	–	25 ppm	84.6 %	[85]
Vapour phase corrosion inhibitors (A) and (B)	9.62 % NaCl + CO_2-saturated with 500 mg/L H_2S, at 70 °C and 500 rpm	Carbon steel	–	50 ppm	97.9 % @ (A) 98.4 % @ (B)	[86]

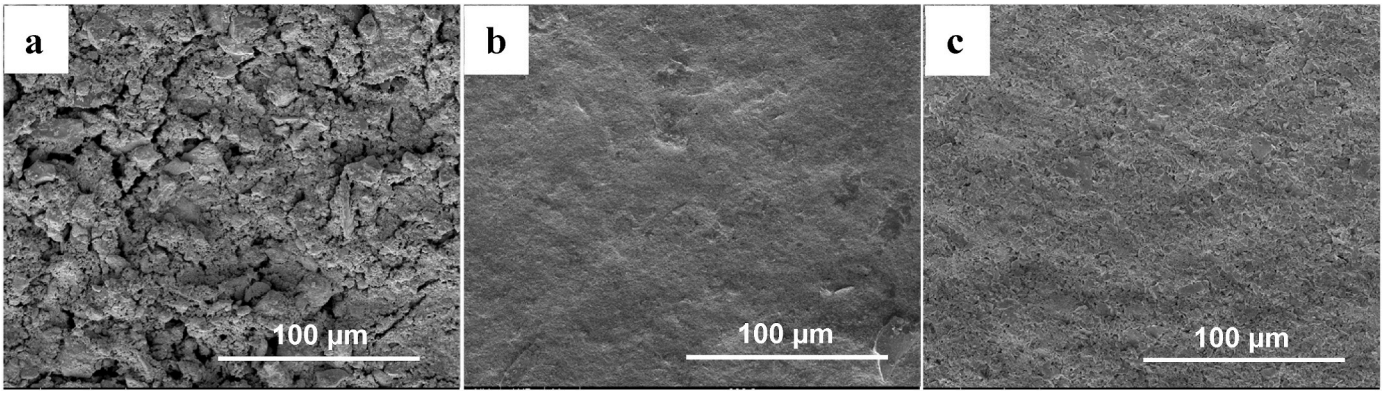

Fig. 7. SEM images of the a) FeS-, b) FeS_2-, and c) SiO_2-covered samples before immersion in the electrolyte.

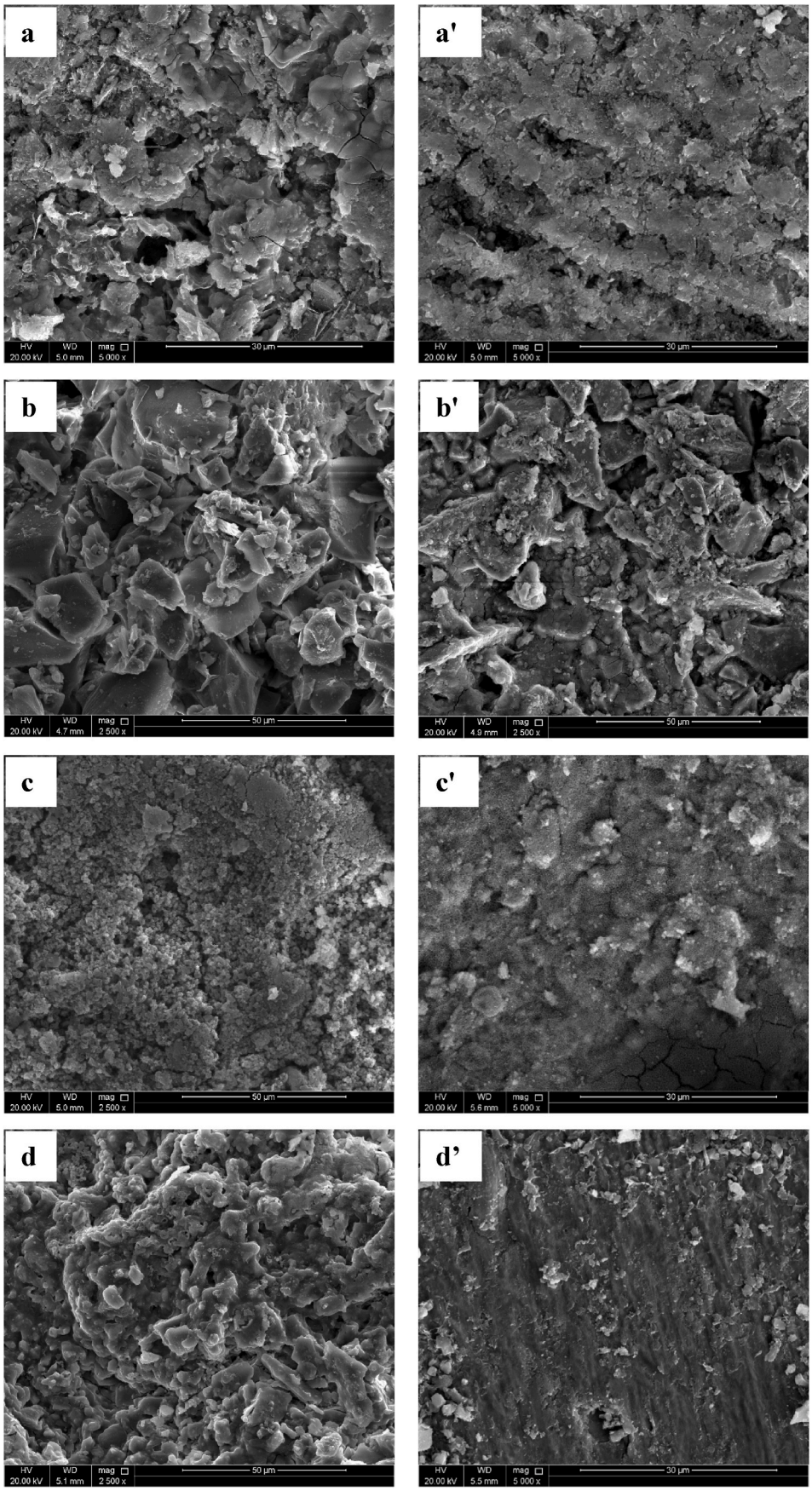

Fig. 8. SEM images of the bare, FeS-, FeS_2-, and SiO_2-covered samples, after immersion in the electrolyte for 24h, in the absence (a, b, c, and d) and presence (a', b', c', and d') of CR11.

Table 5
EDX measurements for the bare, FeS-, FeS_2-, and SiO_2-covered samples, after immersion in the electrolyte for 24h, in the absence and presence of CR11.

Sample	Element	Norm. C (wt.%)	
		In absence of CR11	In presence of CR11
Bare (J55 steel)	C	23.12	31.57
	O	24.76	41.07
	Na	03.96	–
	S	01.68	04.01
	N	–	04.18
	P	–	01.79
	Fe	46.48	17.38
FeS	C	38.67	24.42
	O	29.03	27.26
	Na	03.96	–
	S	03.35	03.17
	N	–	02.18
	P	–	00.59
	Fe	24.99	42.38
FeS_2	C	34.23	39.42
	O	21.93	31.39
	Na	01.79	–
	S	07.68	08.03
	N	–	05.85
	P	–	01.93
	Fe	34.37	13.38
SiO_2	C	21.32	31.48
	O	27.46	38.29
	Na	00.76	–
	S	00.68	01.56
	N	–	09.37
	P	–	02.15
	Si	12.08	11.25
	Fe	37.70	05.90

as shown in Fig. 8 (c' and d'), supporting the higher inhibition of the SiO_2-covered specimens. This is due to the slow diffusion of the inhibitor through the thick layer of FeS_2 and the inertness attitude of the SiO_2. The EDX analysis shown in Table 5 confirms the explanation of the SEM images of both FeS_2- and SiO_2-covered specimens. It is noticed that the presence of N and P peaks in the EDX spectra of the inhibited FeS_2- and SiO_2-covered specimens, as well as the increase in the wt. % of C, O, and S in the inhibited FeS_2- and SiO_2-covered specimens compared to those of the corresponding ones indicate the reaching of the inhibitor to the substrate.

Moreover, the enhancement of the wt. % of N and P in the inhibited SiO_2-covered specimen compared to the corresponding FeS_2-covered one demonstrates the more effortless penetration of the inhibitor through the SiO_2 deposit, giving more inhibition underneath the deposit. Consequently, the SEM/EDX results illustrate that the characteristics of the existing deposit influence the corrosion process. Furthermore, Table 5 confirms that the minimizing wt. % of Fe appearance in the different inhibited specimens' surfaces is in the order of FeS- > deposit free- > FeS_2- > SiO_2-covered specimens. Therefore, the SEM/EDX analysis confirms the acquired data from the EIS measurements and confirms the increase of corrosion resistance of the inhibited steel, especially in the inhibited SiO_2-covered sample that has a protection efficiency of about 99 % after 24 h of immersion in the sulfated sour brine electrolyte, as previously shown in Table 3.

The SEM/EDX mapping on the cross-section of the inhibited FeS_2-covered specimen's surface after 24 h immersion in sulfated CO_2-saturated brine solution is shown in Fig. 9a. Fig. 9 (b, c, d, and f) displays the distribution of each element on the FeS_2-covered sample's surface. The Fe, S, N, and P appear in blue, green, red, and yellow, respectively. The cross-sectional SEM photo verifies the reaching of the inhibitor to the substrate in an irregular distribution around and through the FeS_2 deposit.

Fig. 10 shows SEM images for the deposit free-, FeS-, FeS_2-, and SiO_2-covered samples, after the removal of the corrosion products that are formed after 24h immersion in the electrolyte, in the absence (a, b, c and d) and the presence (a', b', c', and d') of CR11. It is noted that SEM micrographs for the uninhibited and inhibited bare metal surface confirm the uniform corrosion that is usually provided at the steel surface. At the same time, the corresponding deposits-covered specimen surfaces show locally corroded areas reflecting the localized attack at steel underneath deposits, which is more evident in the FeS-covered specimen compared to the FeS_2- and SiO_2 ones. In addition, the inhibited specimens offer less localized corrosion than the corresponding uninhibited ones. Furthermore, the FeS-covered specimen surface demonstrates a more harmful attacked surface than the bare metal, and the most protected surface is shown with the SiO_2-covered specimens.

3.2.2. XPS analysis

Fig. 11 represents the XPS survey spectrum for the deposits-covered specimens before immersion (black) and the inhibited (red) ones after immersion in the sulfated CO_2-saturated brine solution for 24 h. As a

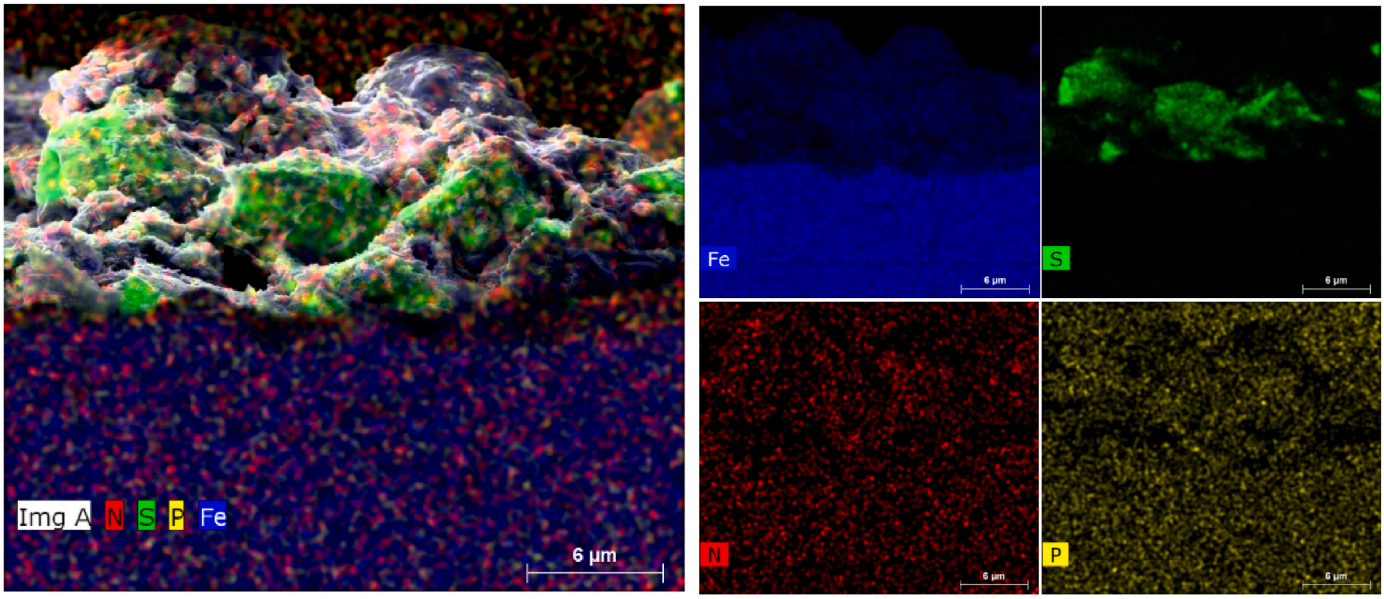

Fig. 9. A representative SEM/EDX mapping of the cross-sectional of the inhibited FeS_2-covered specimen's surface after 24 h immersion in the electrolyte.

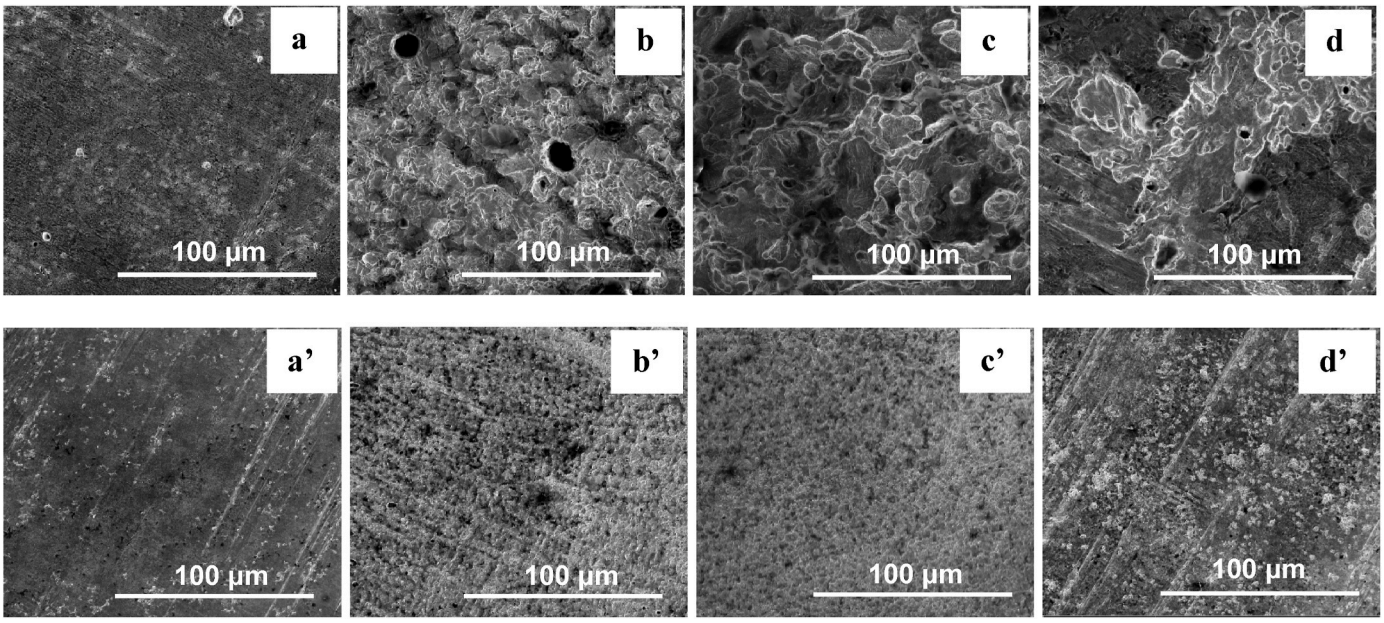

Fig. 10. SEM images for the bare, FeS-, FeS_2-, and SiO_2-covered samples, after removing the corrosion products, in the absence (a, b, c, and d) and presence (a', b', c' and d') of CR11.

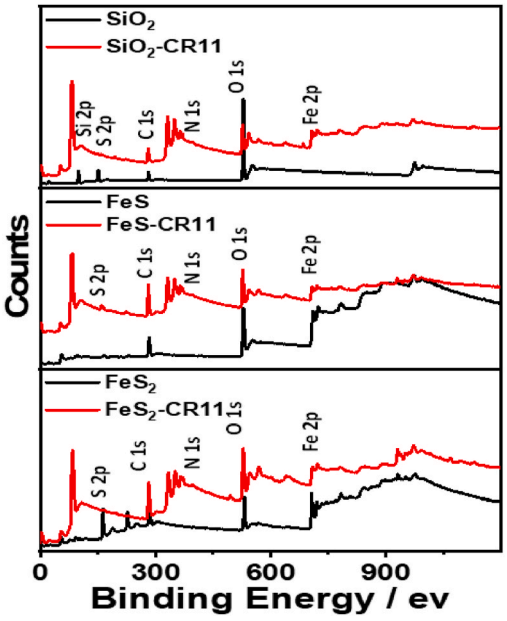

Fig. 11. XPS survey spectrum for the deposits-covered specimens before immersion (black) and the inhibited (red) ones after immersion in the electrolyte for 24 h. (For interpretation of the references to color in this figure legend, the reader is referred to the Web version of this article.)

whole, the broad scan spectrum confirms the presence of Fe 2p, S 2p, C 1s, and O 1s as the main elements in all scans. Meanwhile, the Si 2p peak has been shown in the scan of the SiO_2 deposit, and the appearance of N 1s in the scan of the inhibited deposits-covered specimens proves the reaching of the inhibitor to the substrate.

The high-resolution XPS spectrums for Fe, S, and O in the as-prepared different deposits (FeS, FeS_2, and SiO_2) are shown in Fig. 12 (a, b, and c, respectively). Concerning the XPS spectrum of Fe 2p shown in Fig. 12a, it can be noticed that the benchmarked peaks for Fe 2p are absent in the SiO_2 deposit, which confirms the purity of the silica deposits from any irons contaminations. In the case of FeS, a large peak at 707.5 eV, which is assigned to Fe^{2+}, is shown in the XPS spectrum of the Fe $2p_{3/2}$ region. Moreover, there is a Fe^{2+} satellite peak that appeared at 713.6 eV. The peaks referred to as Fe^{3+} appeared at 709.1 eV, 710.2 eV, 711.3 eV, and 712.3 eV. Fe $2p_{3/2}$ at 707.3 eV and Fe $2p_{1/2}$ at 720 eV are the pyrite peaks dominated high-resolution Fe 2p spectra of FeS_2 [88]. The outcome of emissions from the surface Fe 2p multiplets binding energies at 712 eV, which are explained to come from the slight Fe–S or Fe–O contamination on the surface due to the oxidation of Fe^{2+} to form surface monosulfide, S^{-2}, and Fe^{2+} multiple peaks centered at 708 eV is the high-energy tail seen in the Fe $2p_{3/2}$ spectrum of pyrite [89]. The semiconducting properties of FeS_2 are illustrated by the pyrite value being near that characteristic of metallic iron.

As shown in Fig. 12b, the XPS scan indicated the oxidation states of sulfur in the different deposits. It is noticed that the sulfur content is negligible in the SiO_2 layer while the FeS layer contributions centered at approximately 161.7 eV, which is assigned to elemental iron sulfide (Fe–S. The two fitted peaks position of S $2p_{3/2}$ (S $2p_{1/2}$) at a binding energy of around 161.5 (162.7) and 163.2 eV (164.4 eV) with a full width at half maximum of 1.58 eV for three different deposits represent the presence of stoichiometric FeS and FeS_n (polysulfide). The FeS_2 layer identified as inorganic sulfur-containing minerals (pyrite) at 162.7 eV with an additional peak at 163.5 eV is tentatively assigned to mineral pyrite. The S 2p XPS spectrum of the highest binding energy doublet at 168.2 and 169.5 eV is closely consistent with the nanocube FeS_2 surface due to sulfates, which are believed to be formed by exposure of the pyrite product to air.

Fig. 12c shows the O 1s spectra in the different plain deposits where the area average and individual particles for SiO_2 and FeS were very broad (530–532 eV), suggesting an overlap of contributions from OH^- at 530.7 eV and adsorbed O_2 at 532 eV. Meanwhile, the FeS_2 deposit presents an extra noticeable peak at 529.5 eV as proof of SO_4^{-2} existence.

The high-resolution XPS spectrums for Fe, S, O, C, and N in the inhibited different deposits-covered specimens after immersion in the electrolyte for 24 h are shown in Fig. 13 (a, b, c, d, and e, respectively). Unlike EDX, it isn't easy to quantitatively differentiate between the elements present on the surfaces of the uninhibited and inhibited deposits-covered specimens using XPS analysis. In addition, since the elements that are present on both specimens are almost the same, which are Fe, C, S, and O, forming the same chemical state, except for the presence of N in the inhibited deposits-covered steel, only the high-resolution XPS

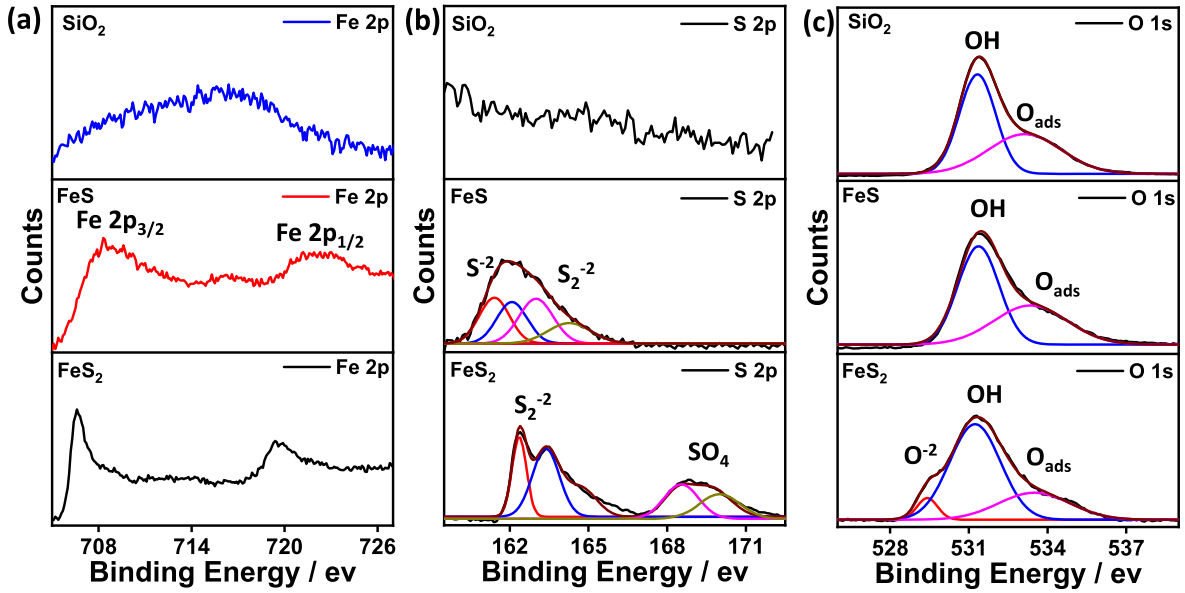

Fig. 12. The high-resolution XPS spectrum for (a) Fe, (b) S, and (c) O in the as-prepared different deposits (FeS, FeS_2, and SiO_2).

spectrum of the inhibited deposits-covered specimens is discussed.

Fig. 13a portrays the XPS spectrum of Fe 2p. Most Fe^{+3} compounds have the complex multiplet-split of Fe 2p regions. Fe $2p_{3/2}$ and Fe $2p_{1/2}$ signals from FeOOH have two peaks at 712.75 and 726.14 eV, respectively. Furthermore, the presence of Fe^{+3} ions in the composite would be confirmed by the satellite peak of Fe $2p_{3/2}$ at 720.83 eV. Moreover, the increased binding energy of the Fe in the XPS of the inhibited deposit-covered steels compared to that of the as-prepared one (Fig. 12a) confirm the formation of $FeCO_3$ at 710.50 eV and $FeSO_4$ at 711.00 eV. When the Fe within the film is in a high-spin state, it would be approved by the presence of the multiplets.

Fig. 13b depicts the S 2p spectrum with a doublet $2p_{3/2}$ near 162.8 eV. However, multiple or a continuum of constituents may produce this high binding energy intensity. For example, it is compulsory for constituents due to pyrite sulfide near 162.4 eV (Fig. 12b) to be present; however, there is an extra intensity at higher binding energy than this value. The assigning of these binding energies to specific species has not been attempted. However, it is claimed that the curve fit can be explained through the amalgamation of pyrite sulfide and adsorbed metal-deficient sulfide.

Initially, the XPS spectra of the FeS were fitted only with the minimum peaks possible. However, these fits were improved when using two doublets for monosulfides and one doublet each for disulfides. The monosulfide species were identified through their binding energies (i.e., 161.1 and 161.8eV). Furthermore, two monosulfide chemical environments were also identified in the mackinawite spectra with FeII–S and FeIII species present. It was impossible to calculate the FeII:S ratios from the XPS spectra due to the significant excess of the sulfur present, which yielded unreasonably high values. The excess sulfur could result from either the presence of excessive polysulfides or indicate a fully saturated sulfur layer on the surface of the analyzed samples. Additionally, there is no intensity in the region of 165–170 eV where S–O moieties are observed; hence, there is no indication of sulfur oxidation on the vacuum-fractured surface.

The O 1s spectrum shown in Fig. 13c can be separated into three prominent peaks, namely, Fe_2O_3 (529.5eV), OH^- (530.7eV), and CO_3^{-2} or SO_4^{-2} (532.2 eV). The occurrence of sulfates can be attributed to the partial oxidation of iron sulfides during the transfer of the sample. Fig. 13d represents the high-resolution XPS spectrum of C 1s. A total of nine different chemical environments for carbon atoms were seen. The deconvoluted peaks of 284.7, 285.5, 286.1, 287.5, 288.2, 289.1, 290.2, 292.7, and 293.9 eV corresponded to, C–C/C=C, C–N, C=N, C–O, C=O, O–C=O, CO_3^{-2}, C–F_2, and C–F_3 bonding, respectively. A significant impact on the shape of the C (1s) spectra is predicted to occur in oxygen functionalities on the carbon surface due to the production of a range of different carbon-oxygen bonds. Fig. 13d portrays the deconvolution results and the high-resolution N 1s spectrum. The peaks at 398.32 and 399.50 eV for C–N and C=N correspond to the mercapto 2-methylimidazole of CR11 corrosion inhibitor. The imidazole ring in 2-methyl imidazole was implied to have a strong interaction with Fe ions disregarding the deposit type due to the variance in the binding energy of imidazole rings. On the other hand, the imidazole ring in the produced ionic liquids did not take part in the complexation. Finally, the XPS results support the obtained EIS data.

4. Conclusion

The performance of different concentrations of UDC commercial inhibitor in sulfated CO_2-saturated brine solution at a temperature of 60 °C and rotation of 1000 rpm in the absence and presence of different deposits is investigated. The impact of the deposits formed on the pipelines and their coverage styles, which are either full or partial, on the corrosion rate of the steel are also illustrated. Electrochemical impedance spectroscopy (EIS) is used to evaluate the deposits and inhibitor' performance electrochemically. Surface analysis using SEM, EDX, and XPS were utilized to illustrate the corrosion mechanism. The main results demonstrated the following:

- The inhibitor offered the highest inhibition efficiency (95 %) in the absence of the deposits at a concentration of 400 ppm.
- In the uninhibited electrolyte solution, FeS_2 offered the highest inhibition efficiency in full and partial coverage throughout the immersion time.
- In the inhibited electrolyte solution, SiO_2 showed the highest inhibition efficiency in both full and partial coverage throughout the immersion time.
- FeS is the highest compatible with the inhibitor whereas FeS_2 is the least one.
- The examined UDC inhibitor can be utilized for inhibition of the UDC caused by FeS and SiO_2 deposit in an aqueous sulfated CO_2 environment. However, it is not preferred to use for impeding the corrosion that is located underneath the FeS_2 deposit.

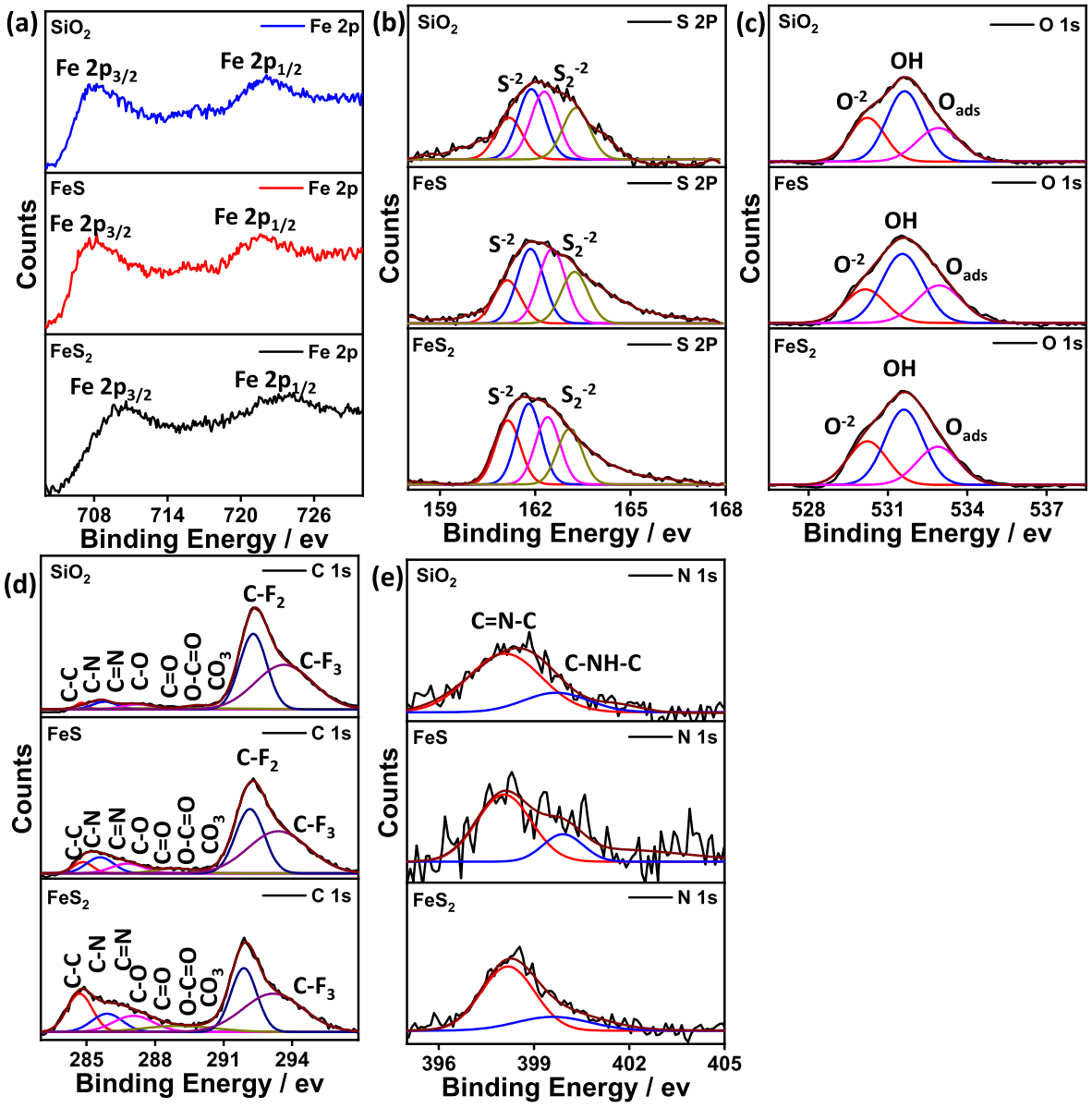

Fig. 13. High-resolution XPS spectrum for the inhibited different deposits-covered specimens after immersion in the electrolyte for 24 h.

- SEM revealed that the deposit-free steel undergo uniform corrosion, whereas the deposits-covered steels are susceptible to localized attack, which depends on the deposit type.
- EDX and XPS confirm the reaching of the inhibitor through the deposits and their adsorption on the steels.

Declaration of competing interest

The authors declare that they have no known competing financial interests or personal relationships that could have appeared to influence the work reported in this paper.

Acknowledgment

This publication was made possible by NPRP grant 13S-0117-200095 from the Qatar National Research Fund (QNRF) (a member of the Qatar Foundation). Statements made herein are solely the responsibility of the authors. This work also is supported by Qatar University through High Impact Grant, QUHI-CAM-22/23–550. The authors would like to acknowledge the Central Laboratory Unit (CLU) efforts, Qatar University, for SEM, EDX analyses, and elemental mapping. The authors also thank the Gas Processing Center (GPC) at Qatar University for conducting the XPS analysis. The publication of this article was funded by Qatar National Library.

Appendix A. Supplementary data

Supplementary data to this article can be found online at https://doi.org/10.1016/j.jmrt.2023.11.244.

References

[1] Wang R, Luo S, Liu M, Xue Y. Electrochemical corrosion performance of Cr and Al alloy steels using J55 carbon steel as base alloy. Corrosion Sci 2014;85:270–9.
[2] Sylvester ON, Celestine ON, Reuben IG, Okechukwu CE. Review of corrosion kinetics and thermodynamics of CO_2 and H_2S corrosion effects and associated prediction/evaluation on oil and gas pipeline system. Int J Sci Technol Res 2012;1:156–62.
[3] Usman BJ, Umoren SA, Gasem ZM. Inhibition of API 5L X60 steel corrosion in CO_2 saturated 3.5% NaCl solution by tannic acid and synergistic effect of KI additive. J Mol Liq 2017;237:146–56.

[4] Hua Y, Barker R, Neville A. Comparison of corrosion behavior for X-65 carbon steel in supercritical CO_2-saturated water and water-saturated/unsaturated supercritical CO_2. J Supercrit Fluids 2015;97:224–37.
[5] López DA, Pérez T, Simison SN. The influence of microstructure and chemical composition of carbon and low alloy steels in CO_2 corrosion. A state-of-the-art appraisal. Mater Des 2003;24:561–75.
[6] Nesic S. Key issues related to modelling of internal corrosion of oil and gas pipelines-a review. Corrosion Sci 2007;49:4308–38.
[7] De Waard C, Lotz U, Milliams DE. Predictive model for CO_2 corrosion engineering in wet natural gas pipelines. Corrosion 1991;47:976–85.
[8] Kashkovskiy RV, Kuznetsov YI, Kazansky LP. Inhibition of hydrogen sulfide corrosion of steel in gas phase by tributylamine. Corrosion Sci 2012;64:126–36.
[9] Finšgar M, Jackson J. Application of corrosion inhibitors for steels in acidic media for the oil and gas industry: a review. Corrosion Sci 2014;86:17–41.
[10] Choi YS, Nesic S, Ling S. Effect of H_2S on the CO_2 corrosion of carbon steel in acidic solutions. Electrochim Acta 2011;56(4):1752–60.
[11] Bai P, Zheng S, Chen C. Electrochemical characteristics of the early corrosion stages of API X52 steel exposed to H_2S environments. Mater Chem Phys 2015;149:295–301.
[12] Salama MM. Influence of sand production on design and operations of piping systems. In: Corrosion 00. NACE International; 2000. p. 80.
[13] Huang J, Brown B, Jiang X, Kinsella B, Nesic S. Internal CO_2 corrosion of mild steel pipelines under inert solid deposits. In: Corrosion 10. NACE International; 2010. p. 379.
[14] Pedersen A, Bilkova K, Gulbrandsen E, Kvarekval J. CO_2 corrosion inhibitor performance in the presence of solids: test method development. In: Corrosion 08. NACE International; 2008. p. 632.
[15] Almahamedh HH. Under-deposit caustic corrosion on sodium carbonate pipeline. Procedia Eng 2015;114:34.
[16] Zhu M, Ou G, Jin H, Wang K, Zheng Z. Top of the REAC tube corrosion induced by under deposit corrosion of ammonium chloride and erosion corrosion. Eng Fail Anal 2015;57:483–9.
[17] Vera JR, Daniels D, Achour MH. Under deposit corrosion (UDC) in the oil and gas industry: a review of mechanisms, testing and mitigation. In: Corrosion 12. Houston, TX: (United states), NACE International; 2012. p. 1379.
[18] Lepková K, Gubner R. Development of standard test method for investigation of under-deposit corrosion in carbon dioxide environment and its application in oil and gas industry. Corrosion 2010. San Antonio, Texas, USA: NACE International; 2010, 10331.
[19] De Reus JAM, Hendriksen ELJA, Wilms ME, Al-Habsi YN, Durnie WH, Gough MA. Test methodologies and field verification of corrosion inhibitors to address under deposit corrosion in oil and gas production systems. Houston, TX, USA: NACE International; 2005, 05288. Corrosion 2005.
[20] Gulieva KK, Mustafaev II, Sabzaliev AA, Garibov RG. Composition and properties of deposits formed on the internal surface of oil pipelines. J Appl Spectrosc 2018;85(1):103–8.
[21] Smith JS, Miller JDA. Nature of sulphides and their corrosive effect on ferrous metals: a review. Br Corrosion J 1975;10(3):136–43.
[22] Rickard D, Luther GW. Chemistry of iron sulfide. Chem Rev 2007;107(2):514–62.
[23] Brown B, Moloney J. Under-deposit corrosion. Trends in oil and gas corrosion research and technologies, production and transmission. Woodhead Publishing Series in Energy; 2017. p. 363–83.
[24] Njoku DI, Li Y, Lgaz H, Oguzie EE. Dispersive adsorption of xylopia aethiopica constituents on carbon steel in acid-chloride medium: a combined experimental and theoretical approach. J Mol Liq 2018;249:371–88.
[25] Dohare P, Ansari KR, Quraishi MA, Obot IB. Pyranpyrazole derivatives as novel corrosion inhibitors for mild steel useful for industrial pickling process: experimental and quantum chemical study. J Ind Eng Chern 2017;52:197–210.
[26] Chidiebere MA, Nnanna L, Adindu GB, Oguzie KL, Okolue B, Onyeachu BI. Inhibition of acid corrosion of mild steel using delonix regia leaves extract. Int Lett Chem Phys Astron 2016;69:74–86.
[27] Oguzie EE, Adindu GB, Enenebeaku CK, Ogukwe CE, Chidiebere MA, Oguzie KL. Natural products for materials protection: mechanism of corrosion inhibition of mild steel by acid extracts of piper guineense. J Phys Chern C 2012;116:13603–15.
[28] Singh P, Ebenso EE, Olasunkanmi LO, Obot LB, Quraishi MA. Electrochemical, theoretical, and surface morphological studies of corrosion inhibition effect of green naphthyridine derivatives on mild steel in hydrochloric acid. J Phys Chem C 2016;120:3408–19.
[29] Haruna K, Obot LB, Ankah NK, Sorour AA, Saleh TA. A green corrosion inhibitor for carbon steel in oil well acidizing environment. J Mol Liq 2018;264:515–25.
[30] Albrakaty RH, Wazzan NA, Obot LB. Theoretical study of the mechanism of corrosion inhibition of carbon steel in acidic solution by 2-aminobenzothiazole and 2- mercaptobenzothiazole. Int J Electrochem Sci 2018;13:3535–54.
[31] Ye QY. In: Study on the mechanism of inhibitor in under-deposit corrosion of carbon steel Ph.D. Thesis. Huazhong University of Science and Technology; 2018.
[32] https://www.outokumpu.com/-/media/files/industries/documents/outokumpu-stainless-steel-for-oil-and-gas-brochure.pdf; 2020.
[33] Sonke J, Grimes WD. Guidelines for corrosion inhibitor selection for oil and gas production. Eurocorr 2016:54317.
[34] Ugur D, Sonke J, Laycock N. Corrosion and corrosion inhibition in wet gas pipelines. Corros Mater 2017;42(1):64–9.
[35] Hassan MSK, Abdullah AM, Ko M, Laycock N, Ingham B, Ryan MP, Williams DE. Effect of Cr/Mo on the protectiveness of corrosion scales on carbon steel in sweet medium under high flow Regime. ECS Trans 2017;80(10):509–17.
[36] Hassan MSk, Abdullah AM, Ko M, Ingham B, Laycock N, Arul R, Williams DE. Local supersaturation and the growth of protective scales during CO_2 corrosion of steel: effect of pH and solution flow. Corrosion Sci 2017;126:26–36.
[37] Shishir CMM, Bernal SA, Provis JL. Chloride-induced corrosion of steel rebars in simulated pore solutions of alkali activated concretes. Cement Concr Res 2017;100:385–97.
[38] Sagoe-Crentsil KK, Glasser FP, Irvine JT. Electrochemical characteristics of reinforced concrete corrosion as determined by impedance spectroscopy. Br Corrosion J 1992;27:113–8.
[39] Etteyeb N, Dhouibi L, Takenouti H, Alonso MC, Triki E. Corrosion inhibition of carbon steel in alkaline chloride media by Na3PO4. Electrochim Acta 2007;52:7506–12.
[40] Criado M, et al. Organic corrosion inhibitor mixtures for reinforcing steel embedded in carbonated alkali-activated fly ash mortar. Construct Build Mater 2012;35:30–7.
[41] Sliem MH, Afifi M, Radwan AB, Fayyad EM, Shibl MF, Heakal FE-T, Abdullah AM. AEO7 surfactant as an Eco-friendly corrosion inhibitor for carbon steel in HCl solution. Sci Rep 2019;9:2319–35.
[42] Shaw BA, McCosby MM, Abdullah AM, Pickering HW. The localized corrosion of AI 6XXX alloys. JOM 2001;53:42–6.
[43] Kaczerewska O, et al. Effectiveness of O-bridged cationic gemini surfactants as corrosion inhibitors for stainless steel in 3M HCl: experimental and theoretical studies. J Mol Liq 2018;249:1113–24.
[44] Ahamad I, Prasad R, Quraishi MA. Adsorption and inhibitive properties of some new Mannich bases of Isatin derivatives on corrosion of mild steel in acidic media. Corrosion Sci 2010;52(4):1472–81.
[45] Emori W, Jiang S, Okonkwo PC, Duan S, Zheng Y. Time- and temperature-dependence of the anticorrosion effect of sodium sulfide on Q235 steel for post-combustion CO2 capture system. Results in Chemistry 2022;4:100300–8.
[46] Abelev E, Sellberg J, Ramanarayanan TA, Bernasek SL. Effect of H2S on Fe corrosion in CO2-saturated brine. J Mater Sci 2009;44:6167–81.
[47] Fayyad EM, Abdul Rasheed P, Al-Qahtani N, Abdullah AM, Hamdy F, Sharaf MA, et al. Microbiologically-influenced corrosion of the electroless deposited NiP-TiNi – Coating. Arab J Chem 2021;14:103445–62.
[48] Nyborg R. Initiation and growth of mesa corrosion attack during CO2 corrosion of carbon steel. Corrosion 98. NACE International; 1998. p. 48.
[49] Biegler T, Rand DAJ, Woods R. Oxygen reduction on sulphide minerals: Part I. Kinetics and mechanism at rotated pyrite electrodes. Electroanal Chem Interfacial Electrochem 1975;60:151–62.
[50] Hilbert LR, Hemmingsen T, Nielsen LV, Richter S. Reliability of electrochemical techniques for determining corrosion rates on carbon steel in sulfide media. Corrosion 2007;63(4):346–58.
[51] Crolet JL, Aquitaine E. In: The role of trace amount of oxygen on the corrosive of H2S media, corrosion 1991. vol. 22. Houston, TX: NACE International; 1991.
[52] Pourbaix A, Aguiar LE, Clarinval AM. Local corrosion processes in the presence of sulphate-reducing bacteria: measurements under biofilms. Corrosion Sci 1993;35(1–4):693–8.
[53] Menendez CM, Jovancicevic V, Ramachandran S, Morton M, Stegmann D. Assessment of corrosion under iron sulfide deposits and CO_2/H_2S conditions. Corros 2013;69(2):145–56.
[54] Huang J, Brown B, Choi YS, Nesic S. Prediction of uniform CO_2 corrosion of mild steel under inert solid deposits. In: Corrosion 11. NACE International; 2011. p. 260.
[55] Been J, Place JD, Crozier B, Mosher M, Ignacz T, Soderberg J, Cathrea C, Holm M, Archibald D. Development of a test protocol for the evaluation of under deposit corrosion inhibitors in large diameter crude oil pipelines. In: Corrosion 11. NACE International; 2011. p. 263.
[56] De Marco R, Jiang ZT, Pejcic B, Poinen E. An in situ synchrotron radiation grazing incidence X-ray diffraction study of carbon dioxide corrosion. J Electrochem Soc 2005;152(10):B389–92.
[57] Ingham B, Ko M, Kear G, Kappen P, Laycock N, Kimpton JA, Williams DE. In situ synchrotron X-ray diffraction study of surface scale formation during CO_2 corrosion of carbon steel at temperatures up to 90°C. Corrosion Sci 2010;52:3052–61.
[58] Huang J. Mechanistic study of under deposit corrosion of Mild steel in aqueous carbon dioxide solution. Ohio University; 2013. Electronic Dissertation Retrieved from: https://etd.ohiolink.edu/.
[59] Wang ZB, Pang L, Zheng YG. A review on under-deposit corrosion of pipelines in oil and gas fields: testing methods, corrosion mechanisms and mitigation strategies. Corro Commun 2022;7:70–81.
[60] Hinds G, Turnbull A. Novel multi-electrode test method for evaluating inhibition of under deposit corrosion-Part 1: sweet conditions. Corrosion 2010;66:046001.
[61] Karim M, Ismail MC, Karim M. Performance of corrosion inhibitor with sand deposit in CO2 environment. ARPN J Eng Appl Sci 2016;11:12103–7.
[62] Brown B, Saleh A, Moloney J. Comparison of mono- to diphosphate ester ratio in inhibitor formulations for mitigation of under deposit corrosion. Corrosion 2015;71:1500–10.
[63] Cui W, Han DD, Zhang XH, Zhang L, Lu MX, Zhong W. CO2 corrosion and the inhibitor effectiveness under sand deposits in offshore pipeline. In: Proceedings of the corrosion 2014 NACE International. Texas, USA: San Antonio; 2014 Paper No. 4183.
[64] He LM, Xu YZ, Wang XN, Huang Y. Understanding the propagation of non-uniform corrosion on a steel surface covered by marine sand. Corrosion 2019;75:1487–501.
[65] Brickell WF, Greco EC, Sardisco JB. Corrosion of iron in an H_2S-CO_2-H_2O system: influence of (single iron) crystal orientation on hydrogen penetration rate. Corrosion 1964;20:235t. –6t.

[66] Smith SN, Brown B, Sun W. Corrosion at higher H_2S concentrations and moderate temperatures. In: Proceedings of the corrosion 2011 NACE International. Texas, USA: Houston; 2011.
[67] Ma HY, Cheng XL, Li GQ, Chen SH, Quan ZL, Zhao SY, Niu L. The influence of hydrogen sulfide on corrosion of iron under different conditions. Corrosion Sci 2000;42:1669–83.
[68] Saremi M, Mahallati E. A study on chloride-induced depassivation of mild steel in simulated concrete pore solution. Cement Concr Res 2002;32:1915–21.
[69] Volpi E, Olietti A, Stefanoni M, Trasatti SP. Electrochemical characterization of mild steel in alkaline solutions simulating concrete environment. J Electroanal Chem 2015;736:38–46.
[70] Valcarce MB, Vázquez M. Carbon steel passivity examined in alkaline solutions: the effect of chloride and nitrite ions. Electrochim Acta 2008;53(15):5007–15.
[71] Böhni H, Uhlig HH. Environmental factors affecting the critical pitting potential of aluminum. J Electrochem Soc 1969;116:906–10.
[72] Zheng H, Li W, Ma F, Kong Q. The performance of a surface-applied corrosion inhibitor for the carbon steel in saturated $Ca(OH)_2$ solutions. Cement Concr Res 2014;55:102–8.
[73] Cellat K, Tezcan F, Beyhan B, Kardaş G, Paksoy H. A comparative study on corrosion behavior of rebar in concrete with fatty acid additive as phase change material. Construct Build Mater 2017;143:490–500.
[74] Pandarinathan V, Lepková K, Bailey SI, Gubner R. Corrosion 13. In: Impact of mineral deposits on CO_2 corrosion of carbon steel. Orlando, Florida: NACE International; 2013. p. 2579.
[75] Pandarinathan V, Lepková K, Bailey SI, Gubner R. Inhibition of under-deposit corrosion of carbon steel by Thiobenzamide. J Electrochem Soc 2013;160(9): C432–40.
[76] Alanazi NM, El-Sherik AM, Rasheed AH, Amar SH, Dossary MR, Al-neemai MN. Corrosion of pipeline steel X-60 under field-collected sludge deposit in a simulated sour environment. Corrosion 2015;71:305–15.
[77] Jenkins A, MacDougall D. Mitigation of under-deposit and weldment corrosion with an environmentally acceptable corrosion inhibitor. In: Proceedings of corrosion 2013 NACE International. Florida, USA: Orlando; 2013 Paper No. 2508.
[78] Tie ZW, Song WW, Zhao JM. Diffusion behaviors of three thioureidoimidazo-line corrosion inhibitors in a simulated sediment layer. Int J Electrochem Sci 2018;13: 5497–512.
[79] Pandarinathan V, Lepkova K, Bailey SI, Gubner R. Evaluation of corrosion inhibition at sand-deposited carbon steel in CO2-saturated brine. Corrosion Sci 2013;72:108–17.
[80] Suarez EM, Machuca LL, Kinsella B, Lepkova K. CO2 corrosion inhibitors performance at deposit covered carbon steel and their adsorption on different deposits. Corrosion 2019;75:1118–27.
[81] Yu N. In: The corrosion mechanism of Oild and gas carbon steel pipelines under deposits Ph. D. Thesis, Huazhong University of Science and Technology; 2014.
[82] Pang L, Wang ZB, Lu MH, Lu Y, Liu X, Zheng YG. Inhibition performance of benzimidazole derivatives with different heteroatoms on the under-deposit corrosion of carbon steel in CO2-saturated solution. Corrosion Sci 2021;192: 109841.
[83] Abd El-Lateef HM, Shalabi K, Tantawy AH. Corrosion inhibition and adsorption features of novel bioactive cationic surfactants bearing benzenesulphonamide on C1018-steel under sweet conditions: combined modeling and experimental approaches. J Mol Liq 2020;320:114564–80.
[84] Onyeachu IB, Njoku DI, Kaya S, El Ibrahimi B, Nnadozie CF. Sour corrosion of C1018 carbon steel and its inhibition by 1–benzylimidazole: electrochemical, SEM, FTIR and computational assessment. J Adhes Sci Technol 2022;36(7):774–94.
[85] Rivera-Grau LM, Casales M, Regla I, Ortega-Toledo DM, Ascencio-Gutierrez JA, Gonzalez-Rodriguez JG, Martinez-Gomez L. H_2S corrosion inhibition of carbon steel by a coconut-modified imidazoline. Int J Electrochem Sci 2012;7(12):12391.
[86] Miksic BM, Furman AY, Margarita AK. Effectiveness of the corrosion inhibitors for the petroleum industry under various flow conditions. CORROSION. Houston, Texas, USA: NACE International; 2009. Paper No. 09573.
[87] Davison W. The solubility of iron sulphides in synthetic and natural waters at ambient temperature. Aquat Sci 1991;53(4):309–29.
[88] Elmi C, Guggenheim S, Giere R. Surface crystal chemistry of phyllosilicates using X-ray photoelectron spectroscopy: a review. Clays Clay Miner 2016;64(5):537–51.
[89] Bai P, Zhao H, Zheng S, Chen C. Initiation and development stages of steel corrosion in wet H_2S environments. Corrosion Sci 2015;93:109–19.